The impact of prior geological knowledge on the interpretation of fracture characterization

A case study of the Buntsandstein formation and crystalline basement in the Upper Rhine Graben

MSc Thesis

T.W. Graafland

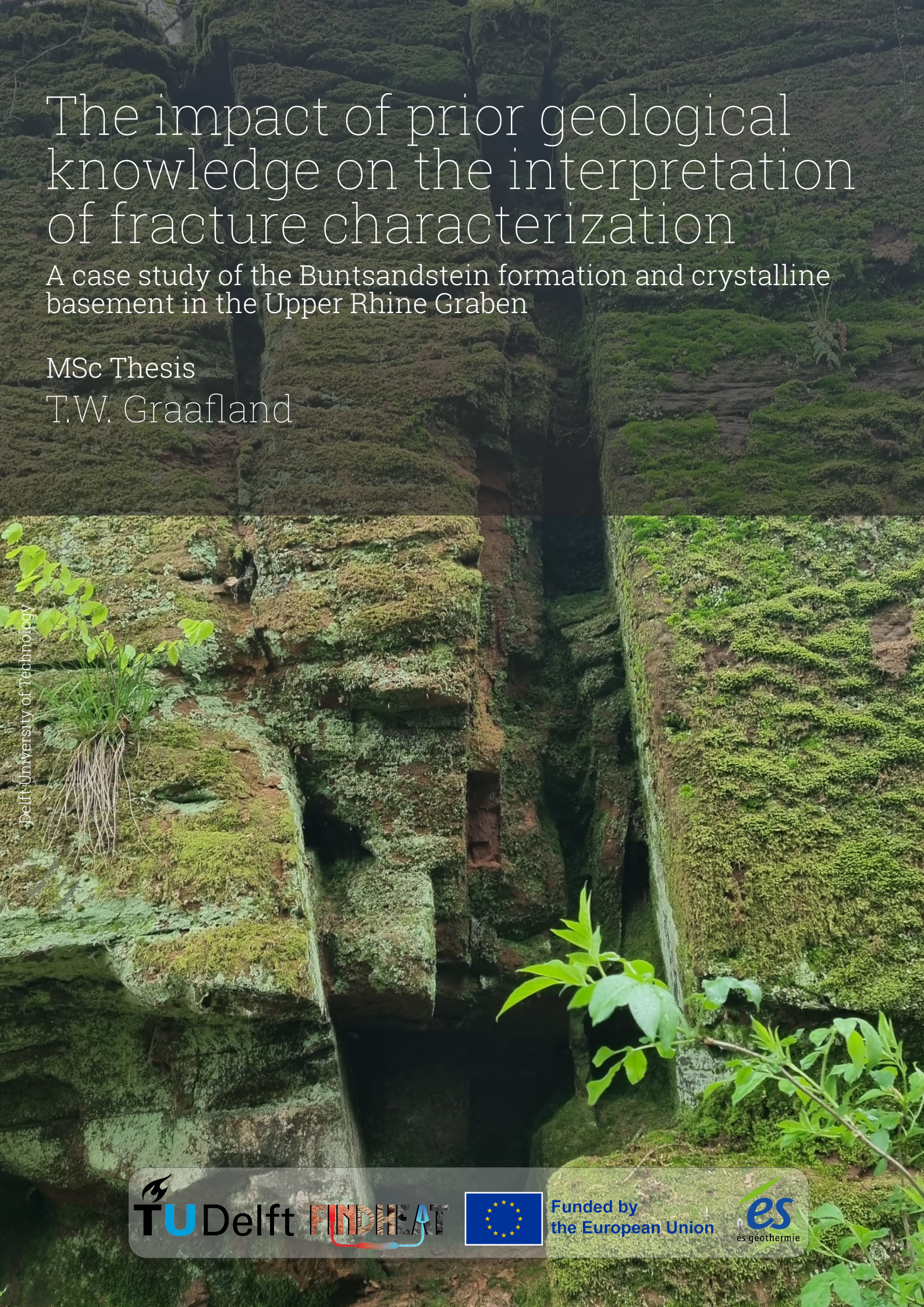

Delft University of Technology

TU Delft FINDHEAT

Funded by the European Union

es géothermie

The impact of prior geological knowledge on the interpretation of fracture characterization

A case study of the Buntsandstein formation and crystalline basement in the Upper Rhine Graben

by

T.W. Graafland

to obtain the degree of Master of Science

at the Delft University of Technology,

to be defended publicly on Thursday July 17, 2025 at 13.45 PM.

Student number:	5145503	
Thesis preparation duration:	November 18 2024 – January 31, 2025	
Thesis duration:	February 1, 2025 – July 17, 2025	
Thesis committee:	Dr. P. B. R. Bruna,	TU Delft, primary supervisor
	Prof. dr. G. Bertotti,	TU Delft, supervisor
	Dr. A. Daniilidis,	TU Delft
	Dr. C. Glaas,	Electricité de Strasbourg Géothermie (ESG)
	Prof. dr. A. Genter	Electricité de Strasbourg Géothermie (ESG)
	V.S. Nogales Herrera	TU Delft

This thesis is confidential and cannot be made public until July 17, 2025

FINDHEAT is a project funded by the European Union's Horizon Europe research and innovation programme under grant agreement No 101147171. Funded by the European Union. Views and opinions expressed are however those of the author(s) only and do not necessarily reflect those of the European Union. Neither the European Union nor the granting authority can be held responsible for them.

TU Delft

Preface

Even though I have always truly enjoyed structural geology, it has never been a subject that came easily to me. Doing my thesis in the field of structural geology has challenged me to push myself and learn new ways of thinking, and I am proud of what I have achieved in the past months.

First off, I would like to thank the FindHeat project and Electricité de Strasbourg Géothermie (ESG) for giving me the opportunity to use their data.

My sincere thanks go to my primary supervisor for the past seven months, Pierre-Olivier Bruna. Thank you for the many brainstorming sessions, pep talks, feedback moments, and overall help. There has barely been a moment when you did not give me the support I needed within a day or two. I could not have wished for a better supervisor during my thesis. Additionally, Giovanni Bertotti has given me the confidence and tools to critically think about my own work, which has greatly improved the end result. Thank you for this.

Furthermore, I would like to thank Carole Glaas and Albert Genter of ESG for both their help during the formative phase of my thesis and for answering all of my questions relating to the image log data, related papers, the GRT-1 well, drilling operations, and the Upper Rhine Graben as a whole.

I would also like to thank Alexandros Daniliidis and Valeria Nogales Herrera for joining the assessment committee. Your feedback during and after my green-light meeting has helped progress my thesis to the work I am proud of today. In addition, I would like to thank Rien Corstanje for his help with WellCAD-related issues and Jasper Hupkens for his help with both WellCAD and coding.

Last but definitely not least, a heartfelt thank you to my family and friends for their unwavering support, not only in the last seven months, but the last six years of my studies.

T.W. Graafland
Delft, July 2025

In this thesis, AI was used according to the guidelines provided by the TU Delft Special Interest Group AI & Assessment (2025).

Abstract

Geothermal energy relies heavily on accurate interpretation of subsurface data to optimize the prediction of the yield and lifetime of a reservoir. Subjective bias remains an overlooked source of uncertainty, even though its significant influence on subsurface data interpretation has been repeatedly proven. This thesis aims to address this subjective bias by providing structured justification for image log and outcrop fracture interpretations. The GRT-1 well at Rittershoffen, France, and the Buntsandstein outcrops in the Vosges region, France, are used as case studies.

A standardized protocol is introduced to provide a structured summary of the expected fractures in the system based on their driving geological processes. The interpreted fractures of three separate interpretations of the GRT-1 well are then linked to these driving processes, after which a composite log of the matching fractures between these is developed. The most prominent and reliable fracture drivers are determined to be the Early Oligocene ENE/SWS extension and the Miocene NW/SE compression. The majority of the picked fractures could be linked to at least one fracture driving process. An overlap in far-field driving processes might indicate reactivation of older fractures.

The protocol offers a promising framework to structure the interpretation of image logs and outcrops. Consequently, discussions on the reliability and justification of the interpretations can be held more constructively, resulting in a more reliable fracture characterization. It is recommended that the protocol be both tested across diverse geological settings and refined to enable more detailed predictions of expected fracture systems.

Contents

Preface i

Summary ii

Nomenclature viii

1 Introduction 1

2 Background 3
2.1 Subjective Bias in Geosciences . . . 3
2.1.1 Types of Subjective Bias . . . 3
2.1.2 Strategies to Reduce Bias . . . 3
2.2 Background Information on Fractures . . . 4
2.2.1 Mode I Fractures . . . 5
2.2.2 Mode II Fractures . . . 5
2.2.3 Hybrid Fractures . . . 5
2.3 Research Area . . . 6
2.3.1 Lithology . . . 7
2.3.2 Variscan Cycle - Paleozoic . . . 7
2.3.3 Alpine/Pyrenean Orogeny - Cenozoic . . . 7
2.3.4 Geothermal History . . . 7

3 Methods 9
3.1 Development and Structure of the Protocol . . . 10
3.2 Image Log Interpretation of GRT-1 . . . 10
3.3 Interpretation of Drivers and Composite Log . . . 11
3.4 Protocol in Fieldwork - 3D . . . 12

4 Protocol Design 13
4.1 Fracture Development in the Far Field . . . 13
4.2 Fracture Development near Planar Faults . . . 13
4.2.1 Damage Zone Thickness . . . 14
4.3 Fracture Development near Listric Faults . . . 15
4.4 Fracture Development in Folds . . . 16
4.4.1 Buckle Folds . . . 16
4.4.2 Forced Folds . . . 16
4.4.3 Fault-related Folds . . . 18

5 Results 20
5.1 Protocol Implementation and Outcomes . . . 20
5.1.1 Far-field Stress Fields . . . 20
5.1.2 Rittershoffen Fault . . . 20
5.2 Image Log Interpretation of GRT-1 . . . 22
5.2.1 Clusters of Fractures . . . 22
5.2.2 Interpretations vs Expected Fractures of Protocol . . . 24
5.2.3 Comparison Different Interpretations . . . 24
5.3 Interpretation of Drivers and Composite Log . . . 24
5.3.1 Permian - ENE/WSW transpression . . . 27
5.3.2 Middle Eocene - N/S compression . . . 27
5.3.3 Late Eocene - NNE/SSW compression . . . 27
5.3.4 Early Oligocene - WNW/ESE extension . . . 27
5.3.5 Late Oligocene - NE/SW compression . . . 27

5.3.6 Miocene - NW/SE compression . . . 27
5.3.7 Residue . . . 29
5.4 Protocol in Fieldwork - 3D . . . 29
5.4.1 Crystalline Basement . . . 29
5.4.2 Buntsandstein . . . 30

6 Discussion **32**
6.1 Interpretation of GRT-1, Drivers, and Composite Log . . . 32
6.1.1 Main Driving Processes . . . 32
6.1.2 Other Driving Processes . . . 32
6.1.3 Variations in Interpretations . . . 33
6.1.4 Comparison GRT-1 and Fieldwork . . . 33
6.2 Effectiveness of Protocol . . . 34
6.2.1 Overlap of Driving Processes . . . 34
6.2.2 Unclassified Fractures . . . 34
6.3 Practical Value of the Protocol . . . 34
6.4 Limitations and Recommendations . . . 35
6.4.1 Development of the Protocol . . . 35
6.4.2 Development of the Composite Log . . . 35

7 Conclusion **37**

References **38**

A Appendix A **42**

B Appendix B **49**

List of Figures

2.1 Structural style vs micro-scale mechanism. Rocks that have brittle deformation on smaller scales might be viewed as ductile at a larger scale (Fossen, 2016) 5
2.2 Full set of discontinuity associations in rigid body deformation (Hancock, 1985; Fossen, 2016; Hupkes et al., 2025) 5
2.3 Research area. A) shows the location of the Rittershoffen geothermal site. B) a vertically exaggerated cross-section of the Rittershoffen and Soultz-sous-Forêts geothermal sites. C) the same cross section without vertical exaggeration. Modified from GeORG (2017). 6

3.1 Overview of the different steps taken in this research. 9
3.2 Difference between an example fracture on FMI and UBI logs. FMI logs have higher vertical resolution, but show a discontinuous image. UBI logs have a lower vertical resolution, but show a continuous image. Note that these are different fractures. 11
3.3 Conceptual drawing of the projected image of a fracture crossing the borehole in 3D (Cruz et al., 2017). 11
3.4 Research area concerning the outcrop locations. The green circles represent locations visited; the Rittershoffen site is visible in the SE corner. 12

4.1 Propagation of fault growth over time (Rotevatn et al., 2019). 14
4.2 Strain localisation increases over time, forming corridors and later faults (Mayolle et al., 2023). 14
4.3 Difference in strain in flexural slip and TLS (Fossen, 2016). 16
4.4 Illustrative summary of fractures founds in buckle folds (Price & Cosgrove, 1990). 17
4.5 Strain and related fractures induced by a forcing fault below the folded rock (J. Cosgrove, 2015). 18
4.6 Formation of fault bend folds (J. Cosgrove, 2015). 19
4.7 Formation of fault propagation folds (J. Cosgrove, 2015) 19

5.1 The pathways of the decision tree taken for the research area of this report. The far-field branch has been repeated multiple times for different driving events. The 'fault' branch has been followed for the Rittershoffen fault. 21
5.2 Schematic drawing of the fracture prediction in the rock around GRT-1 well. The relative intensity of fractures of different orientations and dips is represented in the drawing. . . 22
5.3 Density contour of the poles of the fractures per depth interval and interpretation. For the Buntsandstein and hanging wall of the Rittershoffen fault, you see that the dominant orientation for all interpretations is similar. The spread is wider for deeper rocks. 23
5.4 Cumulative fracture frequency of all interpretations. The fracture frequency is generally constant, but contains clusters of fractures around 1990, 2200-2230, and 2280 meters (MD). 24
5.5 The tadpoles of the fractures picked in all interpretations and composite logs. The composite logs show most matching fractures in the granite. 25
5.6 Cumulative fracture frequency in each of the different interpretations and the composite logs. The Early Oligocene and Miocene are the greatest drivers in most logs. These show the most step-wise increase in cumulative fracture frequency, indicating clusters of these fractures. 26

5.7 Percentage of each driver per depth interval and type of data interpretation. A: The protolith of the crystalline basement has the largest relative share of the Late Eocene driving process. B: The Early Oligocene extension has a variable fraction of fractures in the different interpretations. C: The hanging wall and foot wall in the composite log of two agreements are dominated by the Early Oligocene extension. D: The only driver found in the composite log of three agreements is fractures related to the Miocene compression. 28
5.8 Distribution of the residue fractures after classification of the driving processes for each interpretation. 29
5.9 Examples of different types of fractures present in the crystalline basement (not stimulated). 30
5.10 Fracture clusters at the Falkenstein and Helphenstein Ruin outcrop. 31
5.11 Fracture distribution of protolith of the Buntsandstein. Left: expected fracture distribution. Centre: picked fracture distribution in the FMI log. Right: measured fracture in outcrops. 31
5.12 Distribution of the various driving processes of protolith of the Buntsandstein. Left: expected fracture distribution. Centre: picked fracture distribution in the FMI log. Right: measured fracture in outcrops. The same colour legend as before has been applied. . . 31

A.1 Example of en echelon fractures at tips of an induced fracture 42
A.2 Overview fault orientations and related stress field (Ulutaş, 2020) 43
A.3 Classified into drivers, but no agreements over logs. 47
A.4 Different types of fractures within the Buntsandstein in farfield stress. 48

B.1 Pathway in decision tree: far field stresses as driver 49
B.2 Pathway in decision tree: folds as driver 49
B.3 Pathway in decision tree: planar faults as driver 50
B.4 Pathway in decision tree: listric faults as driver 51

List of Tables

3.1 Observation criteria for FMI and UBI logs for different types of fractures. Generally, in both image logs, the criteria are very similar. It is noted that the higher resolution of the FMI log will likely result in a higher amount of fractures, specifically mode II fractures. . 10

4.1 Overview of the types of fractures expected in the damage zone around a master fault. Related sources: Berg and Skar, 2005; Savage and Brodsky, 2011; Zang et al., 2014; Choi et al., 2016; Fossen, 2016; Peacock et al., 2017; Mayolle et al., 2019; Boersma et al., 2021; Torabi et al., 2020; Smeraglia et al., 2021; Alongi et al., 2022; Mayolle et al., 2023. 14
4.2 Scaling laws for various types of rock. 15
4.3 Overview of fractures expected to be caused by listric fault systems. Related sources: Bally et al., 1981; Williams and Vann, 1987; Buchanan and McClay, 1991; Dula Jr, 1991; McClay and Scott, 1991; McClay et al., 1991; Carr, 1992; Bruhn and Schultz, 1996; Ofoegbu and Ferrill, 1998; Song and Cawood, 2001; Bose and Mitra, 2009; Spahić et al., 2011; Fossen, 2016. 16
4.4 Fractures possibly found related to buckle folding. Related sources: Figure 4.4; Price and Cosgrove, 1990; Cooke, 1997; J. Cosgrove, 1999; J. W. Cosgrove and Ameen, 1999; Sun et al., 2017; Kianizadeh et al., 2021; Wang et al., 2023; Balsamo et al., 2023. 17
4.5 Fractures expected in forced folds with a normal fault or a reverse fault as drivers (Cooke, 1997; J. W. Cosgrove and Ameen, 1999). 18

5.1 The mean, median, and standard deviation of each image log interpretation and the fieldwork data. The FMI has the largest spread in dip angle. The dip of the field data is the highest. 25

A.1 Overview of expected fractures in GRT-1 based on the protocol 44

Nomenclature

Abbreviations

Abbreviation	Definition
GRT-1	injector well Rittershoffen geothermal site
EPS-1	cored well as part of Hot Dry Rock project
URG	Upper Rhine Graben
ECRIS	European Cenozoic Rift System
TVD	True Vertical Depth
MD	Measured Depth
BHI	Borehole Image
FMI	Micro-Resistivity Imaging
UBI	Ultrasonic Borehole Imaging
DZ	Damage Zone
T_{DZ}	Thickness of the damage zone
D	Displacement along a fault plane
HW	Hanging Wall
FW	Foot Wall
TLS	Tangential Longitudinal Strain
DA	Discontinuity Association
LPS	Layer Parallel Shortening
DFN	Discrete Fracture Network
ICM	Image Complexity Map

1

Introduction

Geothermal energy has proven to be a sustainable alternative for heat and electricity generation compared to burning fossil fuels (Bertani, 2009). However, like in all subsurface exploration practices, the data interpretation comes with uncertainty (Witter et al., 2019). Uncertainty in the orientation, spread, and intensity of the fractures often results in wide ranges of possible values regarding directionality, permeability, and connectivity of the reservoir. To constrain these ranges, minimizing uncertainty is necessary to optimize the prediction of the yield and lifetime of the geothermal reservoir.

Uncertainty can be divided into two main categories: objective and subjective biases (Witter et al., 2019). Objective bias is related to factors such as data acquisition and resolution, whereas subjective bias is caused by differences in the interpretation of the data. Identifying the origin and quantifying the former can often be done using statistics, as this is often measurable and reproducible. However, this proves more difficult to do for the latter (Bond et al., 2007).

Subjective bias comes in many forms (Bond et al., 2007; Bond et al., 2015), and these are often categorized in three sub-groups in the geoscience community: (i) anchoring bias - a failure to adjust from an initial idea, (ii) confirmation bias - only seeing data that confirms one's idea, and (iii) availability bias - only seeing the most readily available model in one's mind, for example, the model in which one specializes. As an example, Bond et al. (2007) noted that operators performed better when presented with a seismic dataset within their field of expertise; a synthetic seismic section of a tectonic inversion event was best interpreted by experts who specialize in the structural geology related to tectonic inversion (Bond et al., 2007). The way of thinking of the operator also influences their data interpretation; operators who actively thought about the geologic evolution of a system were more likely to correctly evaluate the synthetic seismic section (Bond et al., 2007). Moreover, the operator's inherent style of data interpretation - or even their personality - has an effect, such as whether they are detail-oriented or only look at the bigger picture (Andrews et al., 2024).

This combined subjective bias manifests not only in the previously mentioned seismic data but also in other types of subsurface data, such as borehole image (BHI) logs. A recent investigation of the manual interpretations from five different operators of the same BHI interval in the Geneva Basin, Switzerland, showed statistically significant variability (Doesburg, 2023). The Geneva Basin is a naturally fractured geothermal target, so this triggers the question of whom to believe for the interpretation of such critical data. Understanding the sources of subjective bias can inform the interpreter of the possible pitfalls during data interpretation.

This thesis suggests that subjective bias can be used to the advantage of the operator. Proper preparation in terms of geological knowledge of the research area and ways of thinking during interpretation of BHI logs can be beneficial for the result, and therefore explain and reduce the uncertainty related to subjective bias. Rather than discrepancies in data interpretation between operators being based on unsupported subjective bias, a protocol is proposed that allows the operator to explain their interpretation and thus pose a stronger argument. This protocol incorporates multiple aspects of the geological history of a system, including tectonic and depositional processes.

The protocol will be tested on image logs of the GRT-1 well in Rittershoffen, France. This well shows the Buntsandstein formation and part of the crystalline basement and is located in the Upper Rhine Graben

(URG). Rittershoffen and the surrounding area have been exploited for geothermal energy since the 1980s, mainly from the highly fractured crystalline basement (Vidal & Genter, 2018). However, the crystalline basement is a deep geothermal reservoir. Drilling comes with significant costs and risks, such as a well collapse - the deeper one drills, the higher these costs and risks become. Therefore, drilling shallower is preferred if the heat potential is similar in the layers above.

In Rittershoffen, recent well tests have suggested similar heat potential in the overlying Buntsandstein formation, which is therefore re-examined. The fracture network in this layer and its connection to the fractures of the crystalline basement might prove insightful for the heat potential of the Buntsandstein. If the Buntsandstein proves to be a viable geothermal reservoir, it will reduce the costs and risks that are involved in drilling deeper towards the crystalline basement. Therefore, proper fracture characterisation is needed.

To complete this research, a baseline of different types of subjective bias and their proposed mitigation strategies is given in chapter 2. Afterwards, an extensive literature study is done to collect the information used to create the protocol. The protocol, which is presented as a decision tree, poses a series of questions on the tectonic history, large-scale structural features potentially driving the occurrence of natural fractures, and the mechanical properties of the rock. These provide insight on the geological constraints on the fractures expected in the BHI log in terms of principal (paleo)stress orientations, the type of fractures, and to some degree the fracture intensity. This is further elaborated in chapter 4.

The fracture distribution of the image logs in GRT-1 is first analysed. The driving processes of fractures expected in GRT-1 are determined based on the protocol. The interpreted fractures from the logs are then classified based on whether they fall within the expected fracture range for each driver. The classified fractures that are present in two or three of the log interpretations are combined in a composite log, which therefore summarizes the most reliable fracture interpretation. The fracture classification is also done on fracture measurements taken from the Buntsandstein outcrops in the Vosges region in France to analyse the applicability of the protocol in outcrops. The full methods approach can be found in chapter 3. Finally, the results are given in chapter 5 and will be discussed and concluded in chapter 6 and chapter 7 respectively.

This thesis is part of the FindHeat project. The FindHeat project aims to ”provide a modular toolkit, the FindHeat platform, which enables a novel geologically-based geothermal resource assessment that minimises the economic and technical risks of geothermal developments, improves the long-term performance of the reservoir, and catalyses a more positive community engagement.”(FindHeat, 2024). The protocol aims to make the interpretation of fracture characterisation in image logs more robust, which is in line with part of the aim of FindHeat (2024).

Research Question

What is the effect of a standardized protocol for linking fractures to driving geological processes on the justification of image log interpretations?

Steps to achieve the research question:

- Create a geologically-constrained protocol to develop better conceptual models of natural fractures in BHI logs;
- Interpret the image logs from GRT-1 in Rittershoffen;
- Classify the fractures based on the expected fracture distribution derived from the protocol;
- Create the composite log of fractures that are present in two or three of the interpretations;
- Compare the classification of fractures for the various interpretations and depth intervals.

2
Background

2.1. Subjective Bias in Geosciences

The importance of identifying and quantifying objective bias and the resulting uncertainty has been widely analysed and adopted in the subsurface exploration industry (Witter et al., 2019). While this analysis greatly improves the viability of an exploration project, the influence of subjective bias on uncertainty has been consistently overlooked in scientific literature (Curtis, 2012; Bárdossy and Fodor, 2001). This is a great concern for fracture characterisation, fracture attributes are picked by people, often by hand, and are therefore inherently biased by the sampling practices of the geologist. A wide range of fracture attributes are therefore sensitive to subjective bias, such as the orientation, trace lengths, degree of clustering, fracture aperture, number of fracture sets, topology, and fracture intensity (Andrews et al., 2019). A non-exhaustive list of types of subjective bias and strategies to mitigate the uncertainty related to these is given in this chapter.

2.1.1. Types of Subjective Bias

Subjective biases are driven by flaws in one or both of the two main processes of decision making: intuitive (Type I) and deliberative (Type II) decision making (Evans & Stanovich, 2013). Type I relies on a heuristic approach to data interpretation, which is obtained from experience and logical thinking (Wilson et al., 2019). Type II supports hypothetical thinking and relies heavily on working memory. This type of thinking supersedes Type I decision making by distinctive higher-order reasoning processes (Evans & Stanovich, 2013), which takes a conscious effort from the decision maker. When Type II thinking does not interrupt and override incorrect Type I thinking, or if Type II thinking itself is faulty or slackened, subjective biases are often introduced (Wilson et al., 2019; Macrae et al., 2016).

Three of the major types of bias discussed in geosciences are anchoring, confirmation, and availability bias, where the latter is suggested to be most common (Bond et al., 2007; Bond et al., 2015). Anchoring bias portrays the difficulty to stray too far from an initial hypothesis, whether this was incorrect or not, even though the evidence might suggest a different outcome (Wilson et al., 2019). Confirmation bias differs slightly; instead of tunnel vision, the decision maker will actively ignore all results that are not in line with their belief. Availability bias arises from a lack of Type II thinking, and focusing only on the model or outcome readily available in one's mind without considering options further from their area of focus (Bond et al., 2007). This type of bias is highlighted by Bond et al. (2015), who suggests the field of expertise influences a (seismic) interpretation more than the level of experience.

A fourth type of bias that is well documented in scientific literature is framing bias. Framing hypotheses in a certain way can influence how one approaches and interprets the results. For example, asking "how good is option X" or "how bad is option X" will possibly yield a different conclusion from the same dataset (Wilson et al., 2019; Alcalde and Bond, 2022). Apart from this, personal influences, such as the decision maker's cognitive style of data interpretation, thought processes, personality, or even state of mind, can create a bias towards the data (Curtis, 2012; Andrews et al., 2024).

2.1.2. Strategies to Reduce Bias

Although subjective bias will likely always be part of the uncertainty related to data interpretation, there are strategies one can apply to minimize the negative effects that subjective bias has on the uncertainty.

Improved use of interpretation techniques

The theory of multiple working hypotheses has been suggested to reduce anchoring and confirmation bias. This strategy forces the decision maker to keep an open mind while interpreting the data (Alcalde & Bond, 2022). Furthermore, Bond et al. (2007) indicates that the greater the number of interpretation techniques used, the more likely the decision maker is to obtain the 'correct' answer to a synthetic seismic section. This can be done by a singular interpreter, but working in a group of people – specifically if this group contains people with different personalities – will obtain better results, decreasing the subjective bias in the final interpretation (Andrews et al., 2019).

Defining conceptual frameworks such as 'thoughts about geological evolution' of the research area will further decrease the subjective bias, as it minimizes the effect of availability bias (Bond et al., 2015; Macrae et al., 2016). Generally, using geological knowledge in every step of data operations (acquisition, processing, analysis, interpretation, and modelling) decreases subjective bias (Pérez-Díaz et al., 2020).

Note that easier interpretations could be done by Artificial Intelligence, such as horizon picking (Petrov et al., 2024). Interpretations normally done through Type I thinking will benefit from this, as the subjective bias caused by personal influences of the decision maker will be reduced (Alcalde & Bond, 2022). However, a human decision maker will still be needed for more creative and complex conceptual model thinking (Type II).

Communicate reasoning for interpretation

Elicitation can be an effective tool to convey reliable information (Curtis, 2012). Elicitation is "the process of expressing expert knowledge in the form of probability distributions for uncertain quantities" (O'Hagan, 2019). Addressing the steps taken in data interpretation, the assumptions made, and the confidence of the decision maker's interpretation quantifies the subjective bias to make the interpretation more transparent and accountable, even if its flaws remain (Soll et al., 2015; Brownstein et al., 2019; Andrews et al., 2019).

Utilization of workflows

To help "capture expert knowledge as objectively as possible" (O'Hagan, 2019), workflows and protocols might prove to be useful tools (Soll et al., 2015). Workflows "nudge" the decision maker in a direction dictated by a compendium of expert judgment, which can induce reflection of the interpretation (Wilson et al., 2019). The workflow reduces availability bias, as multiple hypotheses are proposed and considered (Curtis, 2012). Note that there exists some debate around nudging. Gigerenzer (2015) warns that nudging might only point to the positive effects or results of an interpretation and might lead to the decision maker interpreting the data without a deeper understanding. The author suggests that the decision maker should stay neutral and should only be educated by the workflow to ensure a deeper understanding.

This thesis focuses on a combination of utilizing the geological knowledge of the research area and setting up a workflow to force a deeper understanding of the BHI data through Type II decision making.

2.2. Background Information on Fractures

Fractures form during rigid body deformation of a rock. This means there is movement during deformation without accumulating any internal distortion (Fossen, 2016). Non-rigid body deformation distorts the shape and/or form of the body. Note that this is often a matter of scale; rigid, discrete deformation can be approximated as non-rigid, continuous deformation at a larger scale. In this case, the concept of strain can also be applied to brittle deformation (Figure 2.1). Discontinuity associations (DA) accommodate the rigid body deformation and can include one or more of the following (Figure 2.2; Hancock, 1985; Savage and Brodsky, 2011; Li et al., 2018; Fossen, 2016; Smith et al., 2024; Hupkes et al., 2025):

- Mode I fractures striking perpendicular to σ_3 and often perpendicular to the bedding;
- Mode II fractures in conjugate sets striking parallel to σ_2 and dipping 60° with respect to σ_1;
- Hybrid fractures in conjugate sets striking parallel to σ_2 and dipping 70-80° with respect to σ_1.

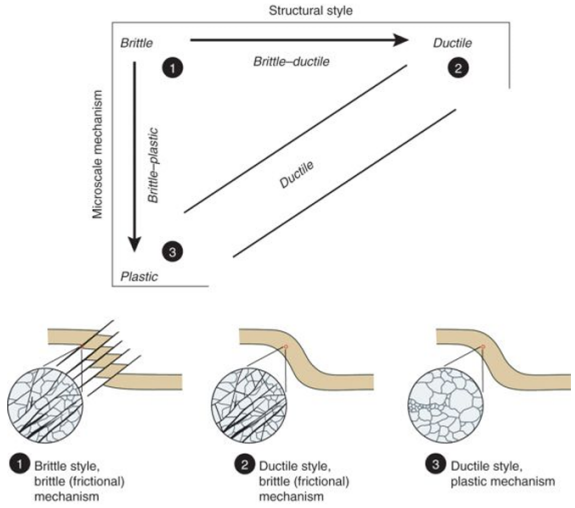

Figure 2.1: Structural style vs micro-scale mechanism. Rocks that have brittle deformation on smaller scales might be viewed as ductile at a larger scale (Fossen, 2016)

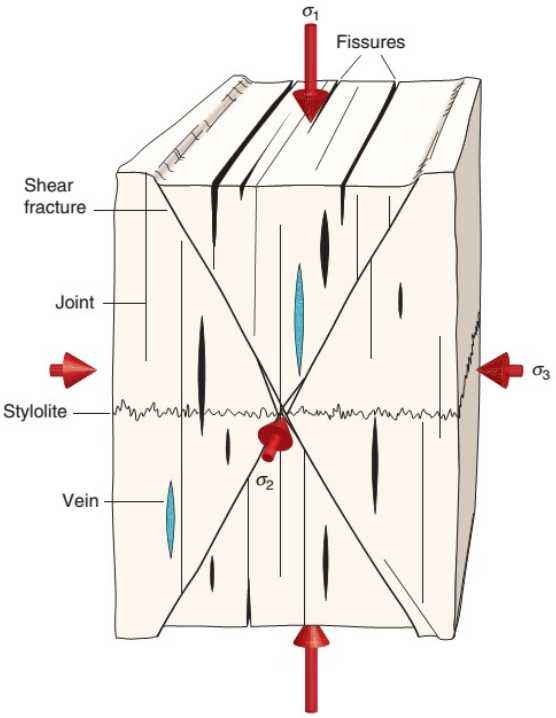

Figure 2.2: Full set of discontinuity associations in rigid body deformation (Hancock, 1985; Fossen, 2016; Hupkes et al., 2025)

2.2.1. Mode I Fractures

Different fracture (and stylolite) orientations might form under the same stress field. Mode I fractures, also known as opening-mode fractures or joints, form by, e.g., micro-scale deformation by grain disaggregation (Mayolle et al., 2023) or splitting of the rock. The fracture plane is perpendicular to σ_3.

2.2.2. Mode II Fractures

A shear fracture, often referred to as a mode II fracture, indicates movement along the fracture plane. Shear fractures can initiate through a series of small-scale en echelon R-fractures (joints) that bend towards and are linked by Y-fractures (shear) (Jacques et al., 2022; Fossen, 2016). These en echelon fractures are, however, rarely visible. Mode II fractures are often hydraulically more open, but mechanically more closed than mode I fractures, which makes these more difficult to observe in BHI logs (Bisdom et al., 2016). Mode II fractures strike parallel to σ_2 and dip approximately 60° to σ_1 (Hancock, 1985). However, there has been quite some debate on the validity of these typical values (Bertotti & Barnhoorn, 2016).

2.2.3. Hybrid Fractures

Hybrid fractures have a dip angle between the typical 60° angle of shear fractures and the vertical dip of opening mode fractures, which raises the debate of the exact differences in the way mode I and mode II fractures are formed (Bertotti & Barnhoorn, 2016). Polymodal fracturing (≥ 3 sets of fracture planes) has been reported in the lab and in outcrops in a wide range of different rock types (Healy et al., 2015 and references therein). The behaviour of polymodal fracturing proves difficult to determine and predict, since the Mohr-Coulomb circle and other similar failure criteria do not account for this type of fracturing. These uncertainties cause a spread in the expected fracture orientations and should be taken into account during fracture interpretation.

Different phases of tectonic activity can be overprinted in rocks, which can make the fracture distribution more scattered. For example, when local stresses had been present in earlier history, caused by e.g.

faults or folds, these fractures might be reactivated and accommodate part of the new regional strain (Skyttä et al., 2021). Vice versa, fractures caused by earlier far-field stresses can accommodate the strain of more recent drivers. This should be taken into account when predicting fracture patterns.

In unstimulated boreholes, the open fractures seen in the BHI logs likely indicate the orientation of the in situ stress field, as these would be induced, reactivated, or not cemented yet (Bisdom et al., 2016). In stimulated boreholes, this is much more difficult to determine; only induced fractures might indicate the in situ stress field. Induced fractures often span over several meters in a borehole and might show en echelon fractures along the edges (Figure A.1)(Hehn et al., 2016).

2.3. Research Area

The main focus of this thesis is the Buntsandstein succession and the top section of the crystalline basement in the GRT-1 well in Rittershoffen, France (Figure 2.3). This well is drilled close to the Soultz-sous-Forêts geothermal site. Both sites are located in the Upper Rhine Graben. It is around 300km long and 30-40km wide. This graben is a typical example of synorogenic continental foreland rifting. Below, the lithological units of primary interest to this study are described, together with the focus points of the tectonic history of the graben.

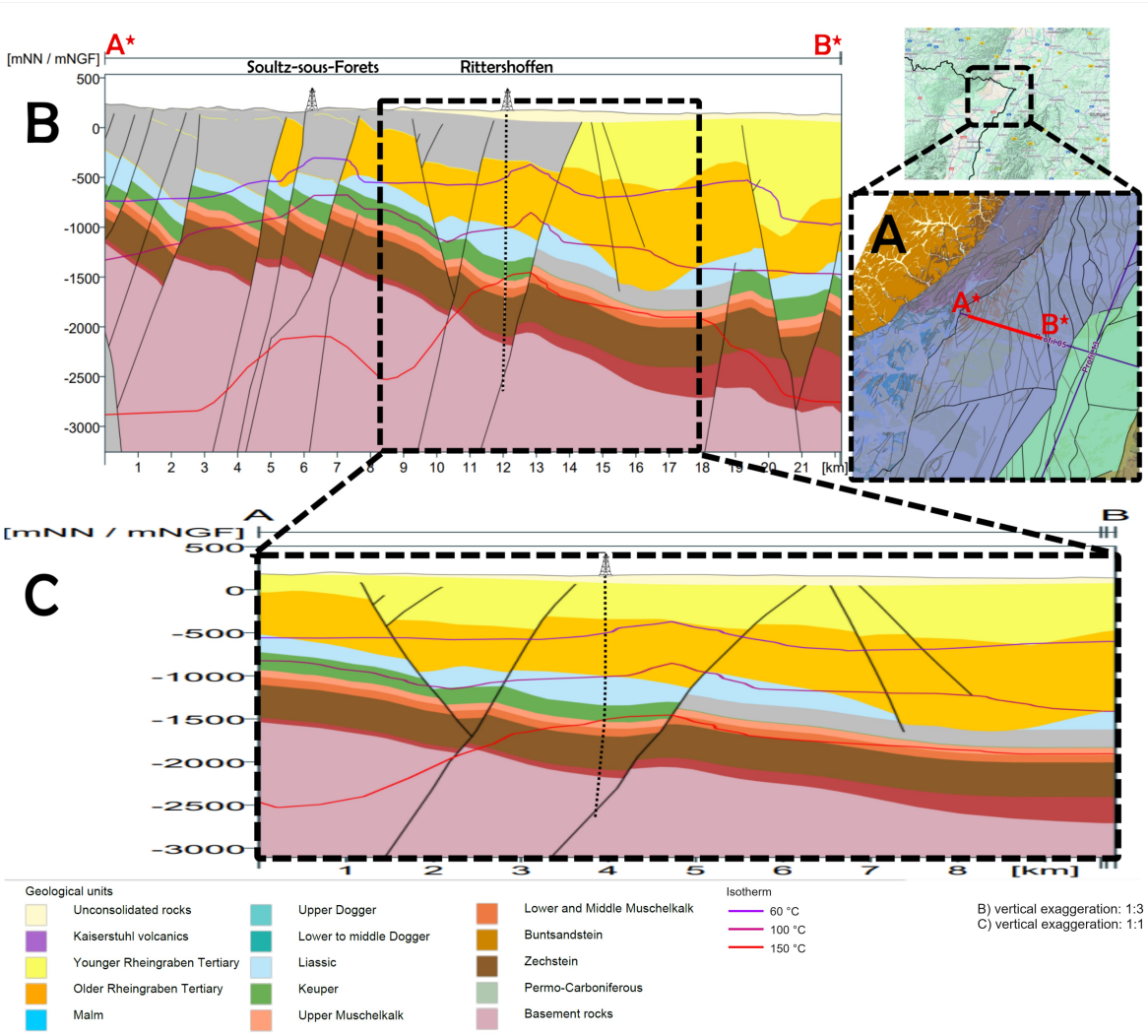

Figure 2.3: Research area. A) shows the location of the Rittershoffen geothermal site. B) a vertically exaggerated cross-section of the Rittershoffen and Soultz-sous-Forêts geothermal sites. C) the same cross section without vertical exaggeration. Modified from GeORG (2017).

2.3.1. Lithology

The upper package of the crystalline basement is a porphyritic, reddish granitic reservoir. It was affected by strong hydrothermal alteration, which intensified upwards (Vidal and Genter, 2018; Glaas et al., 2021). The top of the basement is at 2200m MD in the GRT-1 well. The overlying cover is composed of Triassic sandstones. The Buntsandstein sandstone succession was deposited in the Early and Middle Triassic period. The succession of sedimentological facies is associated with fluvial deposits. The Buntsandstein is divided into four formations: the Annweiler, Vosgian, Intermediate Beds, and Voltzia formation (Vidal & Genter, 2018). The Annweiler, Vosgian, and Intermediate Beds indicate a braided fluvial system, while the Voltzia formation mostly consists of fluvial deposits in a distal alluvial plain environment. All formations form a series of transgression-regression cycles, although they show distinctive patterns which are further elaborated in Vidal and Genter (2018). During and after the deposition of the Volztia formation, a retrogradation of the sediments due to transgression takes place, which transitions to the Muschelkalk succession.

2.3.2. Variscan Cycle - Paleozoic

During the collision of the Laurussia and Gondwana continental plates in the Variscan orogeny, the continental subduction of the Saxothuringian terrane under the Moldanubian terrane in the Late Devonian caused NE-SW striking thrusts close to the region that is now the URG (Baillieux et al., 2013). During the crustal relaxation after the Variscan orogeny (Carboniferous-Permian), intrusive bodies and dyke swarms caused ENE striking highs and troughs, reactivating the ENE striking dextral strike slips faults formed in the later stages of the Variscan orogeny (Schumacher, 2002). The crustal re-equilibration also caused Riedel shear zones striking NNE (Bossennec, 2019). The troughs were overprinted in the Saalian phase due to transpression, which resulted in sinistral NW-SE and dextral E-W conjugate faults (Baillieux et al., 2013; Glaas et al., 2021).

Throughout the remainder of the Mesozoic, tectonic activity was minimal, and burial was the main driver (Baillieux et al., 2013; Glaas et al., 2021).

2.3.3. Alpine/Pyrenean Orogeny - Cenozoic

The Upper Rhine Graben is part of the European Cenozoic Rift System (ECRIS)(Illies, 1972; Vidal and Genter, 2018). The rifting phase can be subdivided into three time periods.

Eocene In the Early Eocene, a N/S compression caused by the Pyrenean collision mostly uplifted the URG area (Dèzes et al., 2004). In the Late Eocene, however, this compression caused a sinistral reactivation of the ENE shear zones from the Late Variscan orogeny (Schumacher, 2002). Towards the end of the Eocene, the compression slightly rotated towards the NNE/SSW.

Oligocene As the NNE/SSW compression lessened relative to the σ_V, the orientation of the principal stress direction shifted at nucleation depth. This WNW/ESE extension marks the start of the rifting phase of the URG (Bossennec, 2019). It is hypothesised that the direction of the URG follows the pre-existing zones of weakness in the crystalline basement, formed by the Riedel shear zones (Dèzes et al., 2004; Glaas et al., 2021). During the Late Oligocene, the graben was reactivated by a phase of NE/SW compression and displayed dextral strike-slip motion.

Miocene Due to the convergence of what is now Africa-Arabia and Europe, the principal stress field underwent a counter-clockwise rotation towards a NW/SE compression. This new principal stress field caused a sinistral strike-slip reactivation of the URG. As a result, restraining and releasing bends are observed in the graben (Schumacher, 2002; Bossennec, 2019).

It is unclear which event has produced the Rittershoffen fault. The present-day stress field is still dominated by the Alpine orogeny. In Rittershoffen, there is NW/SE compression and uplift of 0.5mm/yr (Illies, 1972; Ahorner, 1975; Plenefisch and Bonjer, 1997; Valley et al., 2007; Baillieux et al., 2013).

2.3.4. Geothermal History

The Upper Rhine Graben has been investigated for geothermal exploration since the 1980s. This was initiated by an earlier drilling in Cronenburg done for hydrocarbon exploration. No viable hydrocarbons were found, but a temperature anomaly of 150° was measured at 3220m (Genter et al., 1997). Since then, 15 geothermal wells have been drilled in the region of the URG as part of the scope of various

projects such as the Hot Dry Rock project and the ECOGI project (Vidal and Genter, 2018; Glaas et al., 2021). Thus far, most geothermal projects have focused on the top section of the crystalline basement. However, well tests showed a geothermal gradient of 85-90°C/km for the upper two kilometres in parts of the URG. The temperature anomaly in this area has been interpreted as multi-scale fracture-controlled convective cells (Baillieux et al., 2013; Vidal et al., 2019). Therefore, the Muschelkalk and Buntsandstein successions are looked at as potential geothermal targets.

The GRT-1 well was drilled from September to December 2012 as part of this investigation (Figure 2.3). However, initial well tests showed low injectivity of 0.6 l/s/bar. Therefore, thermal, hydraulic, and chemical stimulation has been performed (Vidal et al., 2016). The injectivity has since increased to 2.6 l/s/bar, which resulted in a nominal flow rate of 70 l/s. It was concluded that GRT-1 has bad connectivity to a medium permeability reservoir, while its counterpart, the deviated well GRT-2, is connected to a high permeability reservoir. The temperature gradient in GRT-1 from the top of the well to the top of the Muschelkalk is 87 °C/km, while the temperature gradient from the top of the Muschelkalk to bottom hole (2580m MD) is only 3°C/km. The bottom hole temperature is 163°C. This confirms the theory of thermal convective cells throughout the Muschelkalk, Buntsandstein, and the crystalline basement (Baujard et al., 2017).

3

Methods

In this research, a protocol is developed that aims to categorize fractures based on various tectonic drivers associated with the research area. This chapter elaborates on the methods approach (Figure 3.1).

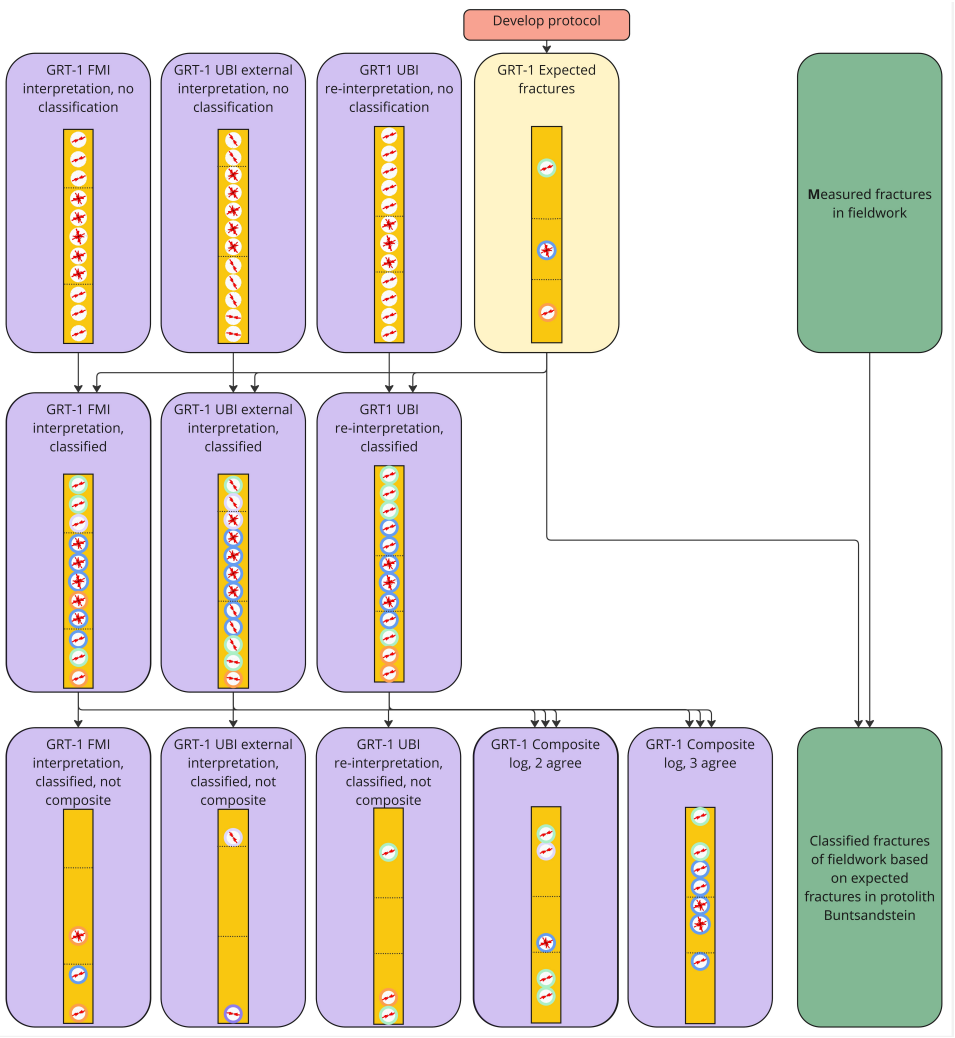

Figure 3.1: Overview of the different steps taken in this research.

3.1. Development and Structure of the Protocol

Based on the tectonic history and geological cross section described in chapter 2, different tectonic drivers of the natural fractures can be deduced. For each driver, the protocol will be followed, resulting in a fracture distribution at a certain depth interval. This protocol, which takes shape as a decision tree, was created based on an extensive literature study and is further elaborated in chapter 4. Also, based on the literature, the expected relative frequency is given.

These are then superimposed to create a prediction of the fracture distribution in the full depth interval of relevance of the GRT-1 well.

3.2. Image Log Interpretation of GRT-1

Two different image logs are analysed: an FMI and a UBI log. Formation Micro-resistivity Imaging (FMI) consists of 16 (4x4) buttons, through which an electrical current runs. These are dragged along the open hole of the well, where the resistivity of the first 2-5mm of the rocks is measured (EPA, 2025). This results in columns of images of high vertical resolution (2.5mm) (Vidal et al., 2016). Variations in resistivity indicate changes in formation or rock properties, and can therefore help identify open or mineral-filled fractures. Open fractures are conductive, since water is more conductive than rock, and will show as dark features in the image logs. In contrast, filled fractures will often have a higher resistivity than the surrounding rock and will appear as light features in the image log. Ultrasonic Borehole Imaging (UBI) rotates a transducer that both emits and receives ultrasonic pulses that reflect off the borehole walls. The amplitude and transit time of the received signal will give information about the formation and consequently about the fractures (SLB, 2025). Table 3.1 summarizes the observation criteria for the transit time and amplitude log. In contrast to FMI, UBI results in a continuous image of the borehole, which simplifies picking fractures (Figure 3.2). The depth of investigation is similar to that for FMI: 2-5mm. However, UBI has a vertical resolution of 10mm, which is significantly larger than that of FMI. Therefore, we expect more thin or small-scale fractures to be picked in the FMI log compared to the UBI log.

Since both UBI and FMI contain logs of a cylindrical borehole, the ‘rolled out’ image will show fractures as sinusoids (Figure 3.3). The amplitude will relate to the dip of the fracture, and the phase of the sinusoid shows the orientation. WellCAD (2024) had been used to analyse the FMI and UBI logs. Here, fractures could be manually picked.

Type of fracture	Observation criteria FMI	Observation criteria UBI
Open mode I	Conductive feature (dark)	Low acoustic signal (dark), high transit time (dark)
	Higher dip angle ($\geq 60°$) Larger mechanical aperture	
Closed mode I (vein)	Resistive feature (light)	High acoustic signal (light), low transit time (light)
	Higher dip angle ($\geq 60°$) Larger mechanical aperture	
Half-open fracture	Often mix of pixels of high and low resistivity	Mix of high and low acoustic signal and transit time Difficult to determine
Open mode II	Conductive feature (dark)	Low acoustic signal (dark), high transit time (dark)
	Variable dip angle Thinner mechanical aperture	
Closed mode II (vein)	Resistive feature (light)	High acoustic signal (light), low transit time (light)
	Variable dip angle Thinner mechanical aperture	
Bedding	Very low angle ($\leq 15°$) Often not a singular line	
Induced fracture	Conductive feature (dark)	Low acoustic signal (dark), high transit time (dark)
	Extremely high dip angles (spanning multiple meters of log) Often asymmetric	
Undetermined	Unclear which of the above fits. Often the case when the difference between bedding and fracture is unclear	

Table 3.1: Observation criteria for FMI and UBI logs for different types of fractures. Generally, in both image logs, the criteria are very similar. It is noted that the higher resolution of the FMI log will likely result in a higher amount of fractures, specifically mode II fractures.

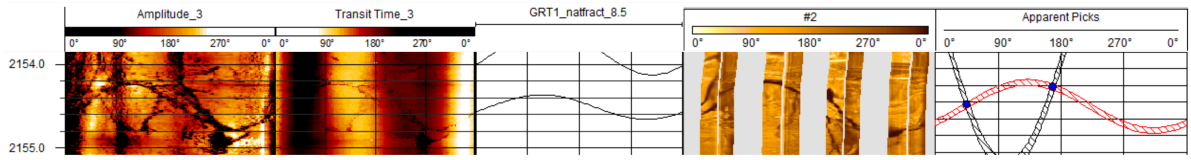

Figure 3.2: Difference between an example fracture on FMI and UBI logs. FMI logs have higher vertical resolution, but show a discontinuous image. UBI logs have a lower vertical resolution, but show a continuous image. Note that these are different fractures.

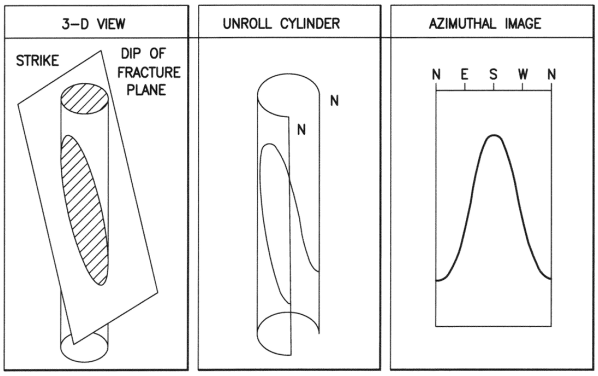

Figure 3.3: Conceptual drawing of the projected image of a fracture crossing the borehole in 3D (Cruz et al., 2017).

3.3. Interpretation of Drivers and Composite Log

A comprehensive list is created based on the protocol to compare the expected fracture orientations to the picked fracture orientations of the different logs. The depth intervals will be used as boundaries for the differences in fracture distribution. After this, the fractures picked in each of the interpretations are compared. It is hypothesized that comparing two interpretations of the same well will result in a composite log that shows the most prominent fractures, which will be the most reliable fracture interpretation. The associated driving processes of these fractures will therefore also be considered to be the most likely dominant fracture driver. Note that multiple driving processes might dominate.

Linking the driving process to the individual fractures is done by filtering the measured fractures based on a range around the expected azimuth and dip given for every driving process in the protocol prediction. For the azimuth, this range is ±15°, while for the dip, a skew range is determined between -10° and +15°. This is to make sure that hybrid fractures are still categorized as mode II fractures in the protocol; mode II fractures now include a range of $50 \leq x \leq 75$°, while mode I fractures are limited to $75 < x \leq 90$ °. The mean fracture dip for mode I fractures is not taken at 90°. This is because the GRT-1 well is a near-vertical well, so most vertical mode I fractures will not cross the well. To compensate for this bias, a mean dip of 85° is taken.

For every fracture, it is investigated what driving event could have produced this. The driving event is only included when at least five fractures can be linked to the driver for each interpretation. It is important to note that fractures are often reactivated by subsequent tectonic events. In some cases, this reactivation is specifically mentioned in the literature. In other cases, the fractures predicted for distinct drivers have an overlap in orientation, which might indicate a reactivation of fractures that were formed in earlier stages. The driver that has the highest expected relative frequency is then picked. If this is similar, the most recent event is picked, though this is further discussed in chapter 6. Some fractures might also not have any predicted driving process that explains the orientation and dip angle. This fracture is then categorized as ‘Residue’.

The FMI and UBI logs, including the driver classification, are then compared to see which fractures are present in both logs and what the associated driving process is. For the composite log, a range is taken that compensates for the spread of azimuth and dip caused by the individual interpreter – the subjective bias. This spread ±15° for both the azimuth and dip angle.

3.4. Protocol in Fieldwork - 3D

Although wells can provide detailed information on individual fractures, they are limited in their spatial extent and do not offer a full 3D view of fracture networks. To obtain a more comprehensive 3D perspective of the effectiveness of the protocol, fieldwork was conducted. This fieldwork was a combination of the analysis of various outcrops and a visual analysis of the cores taken from the EPS-1 well in Soultz-sous-Forêts.

Outcrops have continuously been used as subsurface analogies, also regarding fracture characterisation (Ukar et al., 2019; Ukar et al., 2020). Outcrops of the Buntsandstein succession close to Rittershoffen, France, can be analysed to gain knowledge about the fracture network (Bofill et al., 2024, Figure 3.4). Though the analysed outcrops were close to the research area of GRT-1, they were outside of the damage zone of the closest major fault. Therefore, the protocol has been tested for the far-field geological driving processes present in the undeformed rock of the Buntsandstein.

This will result in a list of fractures measured in the various outcrops, classified based on their respective driving process. The list can be compared to the classification of the fractures of the Buntsandstein interval in the image logs to see whether the protocol yields different results in 1D and 3D fracture networks. Although outcrop analogues are very informative for subsurface reservoirs, these should be interpreted with caution (Bauer et al., 2017; Ukar et al., 2020). The fractures seen in the outcrop might be different than those in the subsurface due to the difference in the recent exhumation and burial history.

The cores of the EPS-1 well provide additional insight into the small-scale (<10 cm) fracture network and clustering of fractures. Moreover, direct observation of the fractures in core samples has supported the interpretation of the image logs.

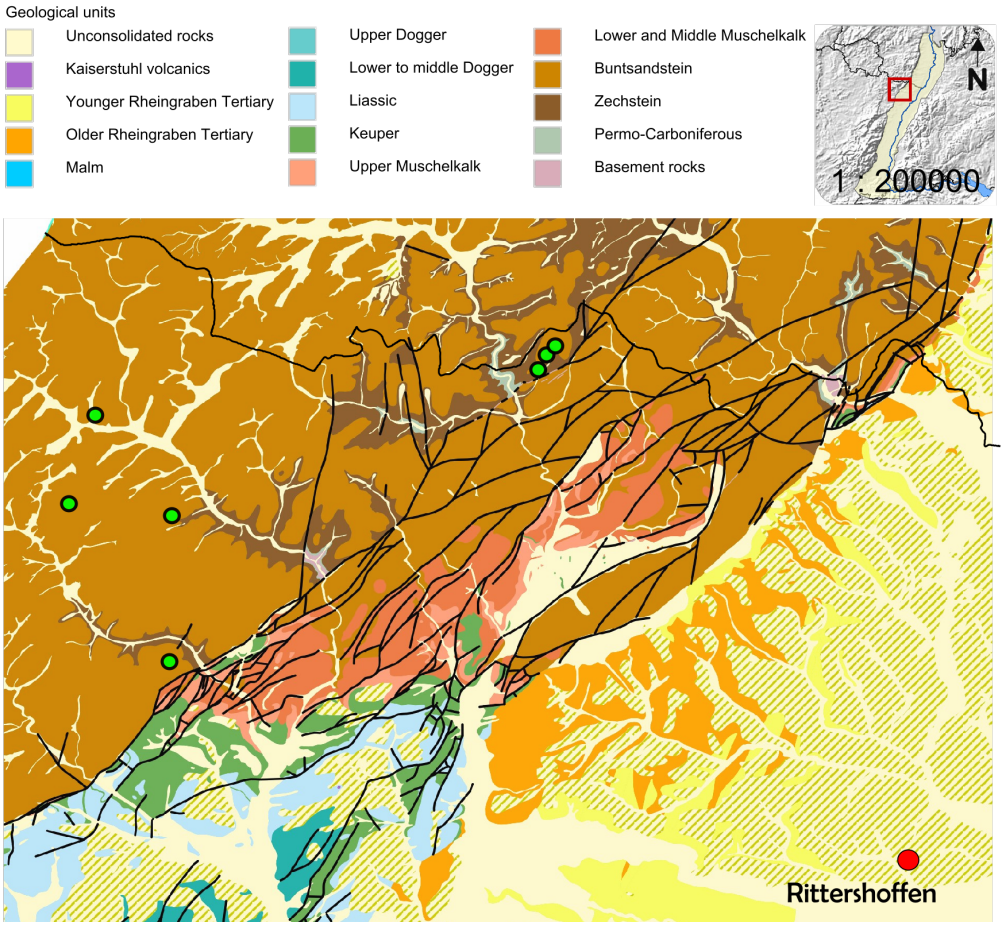

Figure 3.4: Research area concerning the outcrop locations. The green circles represent locations visited; the Rittershoffen site is visible in the SE corner.

4

Protocol Design

An extensive literature review has resulted in a non-exhaustive overview of possible fracture types, orientations, and relative intensities produced by a range of different driving processes behind fractures. The protocol is given in the form of a decision tree and graphical summary in Appendix B. In chapter 5, this protocol is tested and validated through the use of BHI logs and fieldwork data.

4.1. Fracture Development in the Far Field

Far-field stresses are caused by tectonic activity away from the research area. The 'background fractures' belonging to the far-field stress state are found consistently throughout the research area (Berg and Skar, 2005; Savage and Brodsky, 2011; Skyttä et al., 2021; Smith et al., 2024). In extensional regimes, the principal stress orientation is $\sigma_V > \sigma_H \geq \sigma_h$. In compressional regimes, the principal stress orientation is $\sigma_H > \sigma_V \geq \sigma_h$ or $\sigma_H > \sigma_h \geq \sigma_V$, which is the driving force behind layer parallel shortening (LPS). One or more of the fractures mentioned in the DA above can be formed. Each of these fractures individually can point to a certain stress orientation, though multiple sets of the DA's provide a stronger argument for this. Note that the joints might be difficult, if not impossible to observe, if the $\sigma_3 = \sigma_V$, as these will be parallel to the bedding, assuming the bedding is horizontal.

4.2. Fracture Development near Planar Faults

Faults are complex and heterogeneous features (Torabi et al., 2019). However, faults are often simplified as planar features with a fault core, damage zone (DZ), and protolith (Caine et al., 1996). The protolith indicates the part of the rock not influenced by fractures related to the fault, but is likely still deformed by the far-field stresses. Pre-existing structures and boundary conditions, such as the magnitude of the principal stress field, influence the development of master faults and their associated damage zones (Childs et al., 2017). The DZ is formed as the fault is initiated and the rock starts to displace, and includes smaller secondary faults, veins, fractures, cleavage, and possibly folds (Caine et al., 1996). It is suggested that far-field stresses can create fracture clusters that are structured and closely spaced, otherwise known as fracture corridors (Schueller et al., 2013; Souque et al., 2019). While the strain continues to increase, a master fault might be formed by linkage of smaller segments in fracture corridors: strain localisation (Figure 4.1; Figure 4.2; (Mayolle et al., 2023)). This is why smaller fracture clusters in the area of a master fault often have a similar orientation to the master fault.

Planar faults can be classified as normal, strike-slip, or thrust faults, depending on the orientation of the principal stresses (Fossen, 2016). Although these fault types differ in kinematics, they can produce similar fracture networks when viewed in their respective stress regimes (Figure A.2; Childs et al., 2017). This research is written from the perspective of normal faults, though after re-orientation can be used in strike-slip and thrust faults.

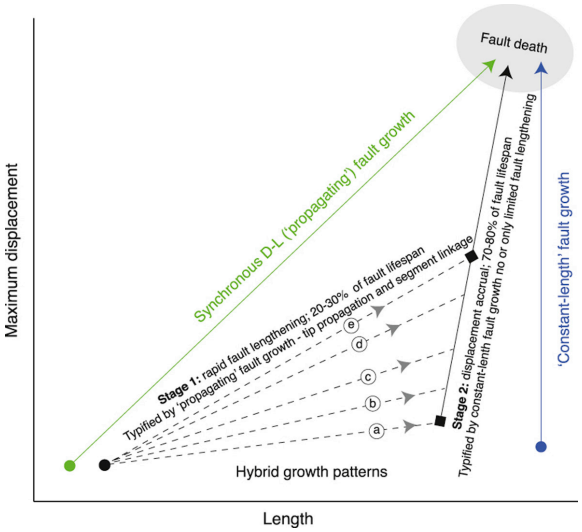

Figure 4.1: Propagation of fault growth over time (Rotevatn et al., 2019).

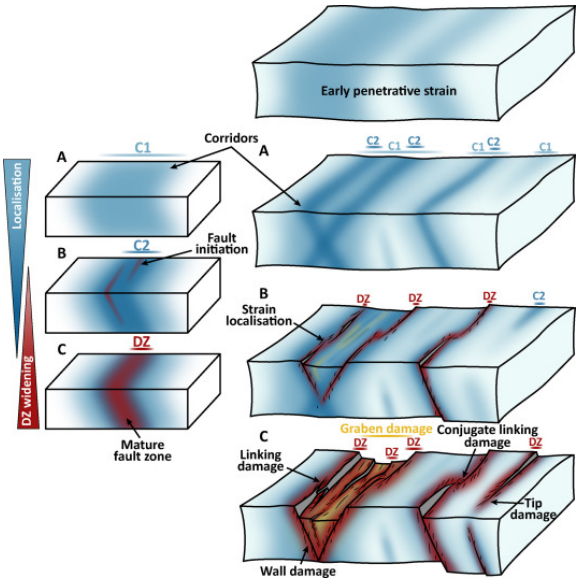

Figure 4.2: Strain localisation increases over time, forming corridors and later faults (Mayolle et al., 2023).

It has been widely recorded that fracture frequency logarithmically decreases away from the fault core (Savage and Brodsky, 2011; Schueller et al., 2013; Mayolle et al., 2019). Quantifying the fracture frequency based on the displacement of the fault (D) is extremely challenging and currently outside the scope of this research. However, the relative fracture frequency, orientations, and types of fractures can be estimated based on the available literature.

Fractures around the master fault plane in the DZ are known as cross-fault damage, while fractures directly caused by the fault plane are known as along-fault damage (Y. S. Kim et al., 2004; Choi et al., 2016). Fractures in the along-fault damage zone are subdivided into linking damage, tip damage, and wall damage (Y. S. Kim et al., 2004). The fracture orientations related to this are summarized in Table 4.1.

Where	Type	Orientation strike (w.r.t master fault)	Dip (w.r.t bedding)	Notes
DZ	mode I	30°	perpendicular	Follow farfield stress field, found more in sedimentary deposits
DZ	mode II	parallel	60° (or same as master fault)	Found more in tight, hard rocks
DZ	hybrid	parallel	70-80°	Found more in tight, hard rocks
Linking between faults	mode I	often perpendicular	-	Mode I and rotated blocks, but rarely seen
Tip of fault	wingcracks and horsetail fractures	30°, though variable	-	
Tip of fault	mode II	parallel	60° (or same as master fault)	Synthetic branches or antithetic faults
Wall of fault	mode I	30°, though variable	-	En echelon fractures
Wall of fault	-	-	-	Can overprint older tip and linking damage
Hanging wall DZ	mode II	parallel	60° (or same as master fault)	Mostly antithetic fractures
Hanging wall DZ	mode II	(sub)perpendicular	30°	Thrust faults, though rarely present
Foot wall DZ	mode II	parallel	60° (or same as master fault)	Mostly synthetic fractures
Foot wall DZ	mode II	(sub)perpendicular	30°	Thrust faults, though rarely present

Table 4.1: Overview of the types of fractures expected in the damage zone around a master fault. Related sources: Berg and Skar, 2005; Savage and Brodsky, 2011; Zang et al., 2014; Choi et al., 2016; Fossen, 2016; Peacock et al., 2017; Mayolle et al., 2019; Boersma et al., 2021; Torabi et al., 2020; Smeraglia et al., 2021; Alongi et al., 2022; Mayolle et al., 2023.

4.2.1. Damage Zone Thickness

Many papers have attempted to create scaling laws between the displacement of the fault and the thickness of the damage zone for different fault properties (Choi et al., 2016). These scaling laws are

rough approximations, but might give useful information to estimate the relative intensity and orientation of the fractures in wells.

The damage zone thickness (T_{DZ}) is mostly dependent on the rock type and displacement along the master fault. The T_{DZ}/D scaling flattens and eventually stabilizes around T_{DZ} of some 100s of meters at a certain (highly debated) value of D. Schueller et al. (2013) and Mayolle et al. (2019) put this threshold of D at 150m, though Choi et al. (2016) takes roughly 1 km as the threshold. This stabilization is likely due to the distribution of slip onto secondary strands within the DZ; the superposition of multiple locations of fracturing is often referred to as secondary fault strand nucleation (Savage & Brodsky, 2011). Scaling laws for displacement <1km differ for various rocks of various mechanical properties (Table 4.2).

Type of rock	DZ	Scaling law	Literature	Notes
Carbonates	full DZ	$T_{DZ} = 1.6D^{0.82}$	(Mayolle et al., 2019)	
Porous siliciclastic rock	foot wall	$T_{DZ} = 1.2564D^{0.48}$	(Choi et al., 2016)	slightly different for different porosities (Congro et al., 2023; O'Hara et al., 2017)
Porous siliciclastic rock	hanging wall	$T_{DZ} = 1.0245D^{0.6433}$	(Choi et al., 2016)	slightly different for different porosities (Congro et al., 2023; O'Hara et al., 2017)
Tight rock	foot wall	$T_{DZ} = 10.141D^{0.2002}$	(Choi et al., 2016)	
Tight rock	hanging wall	$T_{DZ} = 4.5652D^{0.5471}$	(Choi et al., 2016)	

Table 4.2: Scaling laws for various types of rock.

Although these are the values used in this research, it is important to note that not all research draws similar conclusions. Alongi et al. (2022) shows no substantial difference in trends of T_{DZ} in the hanging wall and foot wall and shows a damage zone in the order of 1-2km in magnitude. Future research will provide more insight into this. It is recommended to be mindful that the master fault is part of the evolving system that is the Upper Rhine Graben, hence the damage zone should not be looked at as relating to a singular planar fault (Mayolle et al., 2019). Rather, the damage zone is a complex fracture network that changes with changing strain.

4.3. Fracture Development near Listric Faults

Listric faults can be approximated as planar faults in brittle structures, where the dip becomes shallower as the ductility of the rock increases. Most normal master faults become listric faults around 5-17km depth, where a zone of low velocity exists (Shelton, 1984). Various fractures can be present in the damage zone of listric faults specifically. These are summarized in Table 4.3 and further elaborated in this section.

Listric faults can form in a domino-style sequence with one master fault and secondary listric faults in the hanging wall (Ofoegbu & Ferrill, 1998). These faults might be linked by large-scale synthetic Riedel fractures (Zhao et al., 2020). The hanging wall is often a drag fold, accommodating most of the strain, indicating that the bedding steepens towards the fault plane (Bally et al., 1981).

The fault plane of listric faults has been theorized to consist of relatively short, en echelon fracture segments. These fractures, together with the irregularity of the grooves in the fault plane of listric faults, increase the spread of orientations of the associated fractures (Shelton, 1984). Stresses at the tip of the fault are generally less intense due to the shallow angle, so the tip damage is less prevalent (Resor & Pollard, 2012). Since roll-over folds have traditionally been looked at for hydrocarbon exploitation, the foot wall has been studied significantly less than the hanging wall, so the properties of the fracture network were less widely known.

Where	Type	Orientation (w.r.t master fault)	Dip (w.r.t horizontal)	Notes
Fault plane	en echelon segments	parallel	approx. 30° w.r.t. fault plane	-
Hanging wall	mode II	parallel	steep >70°	mostly antithetic some synthetic
Hanging wall Syn-rift sediments	mode II	parallel	steep >70°	less fractured
Foot wall	Mode II	parallel	more shallow <60°	mostly synthetic some antithetic

Table 4.3: Overview of fractures expected to be caused by listric fault systems. Related sources: Bally et al., 1981; Williams and Vann, 1987; Buchanan and McClay, 1991; Dula Jr, 1991; McClay and Scott, 1991; McClay et al., 1991; Carr, 1992; Bruhn and Schultz, 1996; Ofoegbu and Ferrill, 1998; Song and Cawood, 2001; Bose and Mitra, 2009; Spahić et al., 2011; Fossen, 2016.

4.4. Fracture Development in Folds

Folds can accommodate strain as flexural slip or tangential longitudinal strain (TLS) (Figure 4.3; J. Cosgrove, 2015). Layers will 'slide' along layer boundaries during flexural slip, while strain is accommodated through fractures crossing layers in TLS. Most fractures form at the hinge instead of the limbs when TLS is the dominant type of strain accommodation. In reality, there is an interplay between these types of accommodation, which might make the fracture pattern very complex (J. Cosgrove, 2015; Balsamo et al., 2023.

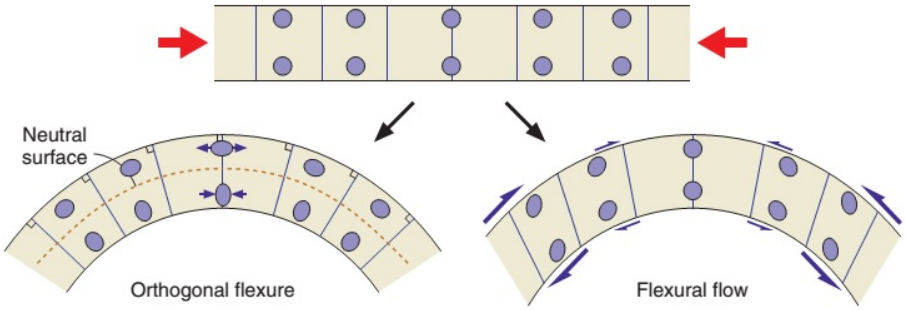

Figure 4.3: Difference in strain in flexural slip and TLS (Fossen, 2016).

4.4.1. Buckle Folds

Buckle folds form with the principal stresses (sub) parallel to the bedding and are initiated right after LPS (J. Cosgrove, 1999). Bazalgette et al. (2010) has suggested that folds frequently need a pre-existing structure as an initiation point. These structures can either be pre-existing faults or fracture corridors (sub) parallel to the future fold hinge that extend to most of the mechanical unit thickness. Note that this is a comprehensive overview of the types of fractures and fracture orientations one can expect in a buckle fold, though this does not mean that all of these will be present in every fold. Table 4.4 and Figure 4.4 give an overview of the expected fractures.

4.4.2. Forced Folds

The overall shape and trend of forced folds are dominated by the shape of some forcing member below (J. W. Cosgrove & Ameen, 1999). This forcing member can range from salt diapirs to faults, though this research focuses only on the latter. Normal and reverse faults can occur in members below, causing strain in the members above and a chaotic associated fracture pattern (Figure 4.5, Table 4.5).

Where	Type	Orientation (w.r.t fold hinge)	Dip	Notes
Top of hinge	splay cracks	parallel	shallow dip (variable)	splay from bedding parallel fractures
Top of hinge	mode I	(sub) parallel	perp. to bedding	-
Top of hinge	cross-joints	(sub) perpendicular	perp. to bedding	-
Top of hinge	mode II/hybrid	<30°	perp. to bedding	if locally $\sigma_1 = \sigma_H, \sigma_2 = \sigma_V, \sigma_3 = \sigma_h$
Top of hinge	mode II/hybrid	(sub) parallel	oblique to bedding	if locally $\sigma_1 = \sigma_V, \sigma_2 = \sigma_H, \sigma_3 = \sigma_h$
Bottom of hinge	mode II/hybrid	parallel	<30° to bedding	Rare
Limbs	mode I	(sub) parallel	perp. to bedding	fracture intensity lower
Limbs	cross-joints	(sub) perpendicular	perp. to bedding	fracture intensity lower
Limbs	mode II/hybrid	<30°	perp. to bedding	if locally $\sigma_1 = \sigma_H, \sigma_2 = \sigma_V, \sigma_3 = \sigma_h$, fracture intensity lower
Limbs	mode II/hybrid	(sub) parallel	oblique to bedding	if locally $\sigma_1 = \sigma_V, \sigma_2 = \sigma_H, \sigma_3 = \sigma_h$, fracture intensity lower

Table 4.4: Fractures possibly found related to buckle folding. Related sources: Figure 4.4; Price and Cosgrove, 1990; Cooke, 1997; J. Cosgrove, 1999; J. W. Cosgrove and Ameen, 1999; Sun et al., 2017; Kianizadeh et al., 2021; Wang et al., 2023; Balsamo et al., 2023.

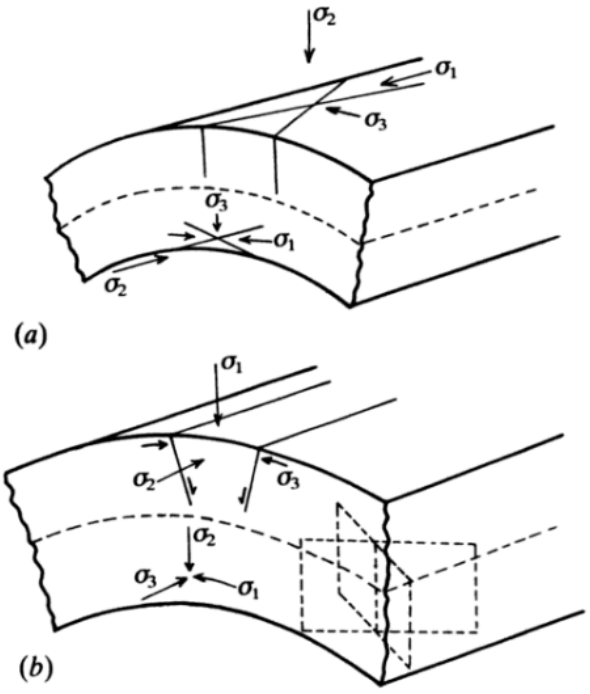

Figure 4.4: Illustrative summary of fractures founds in buckle folds (Price & Cosgrove, 1990).

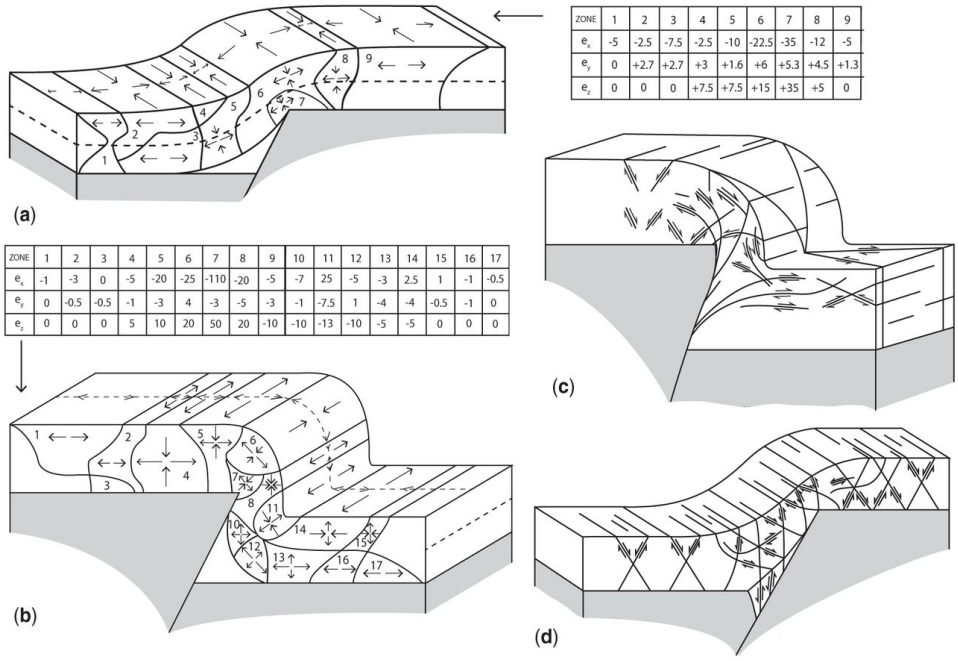

Figure 4.5: Strain and related fractures induced by a forcing fault below the folded rock (J. Cosgrove, 2015).

Where	Type	Orientation (w.r.t. strike master fault)	Dip (w.r.t. bedding)	Notes
Hinge	mode I	parallel	perpendicular	Curvature-related fractures
Hinge	splay cracks	parallel	shallow dip (variable)	Splay from bedding parallel fractures, rare
Tip of fault	-	-	-	Chaotic fracturing
Normal fault forcing	mode II	parallel	60°	Both syn- and antithetic
Reverse fault forcing	mode II	parallel	60°	Both syn- and antithetic
Reverse fault forcing, foot wall	mode II	parallel	30°	Thrust

Table 4.5: Fractures expected in forced folds with a normal fault or a reverse fault as drivers (Cooke, 1997; J. W. Cosgrove and Ameen, 1999).

4.4.3. Fault-related Folds

A fault-related fold is the dragging of bedding with fault displacement (Suppe & Medwedeff, 1990). Fault bend folds are formed by the movement of bedding along a series of connected faults (Figure 4.6). These faults are bedding parallel fractures following weaker layers before 'jumping' up to a higher weak layer in the bedding. This jump of 30° is called a ramp, and the bedding parallel fractures are flats (J. Cosgrove, 2015). At every hinge in the fault bend fold, similar patterns to the ones found in buckle folds are formed. Every transition from a flat to a ramp forms a new fold hinge. The overprinting of the fractures gives rise to a very complex fracture pattern (Price and Cosgrove, 1990; Suppe and Medwedeff, 1990; Hardy and Allmendinger, 2011; J. Cosgrove, 2015).

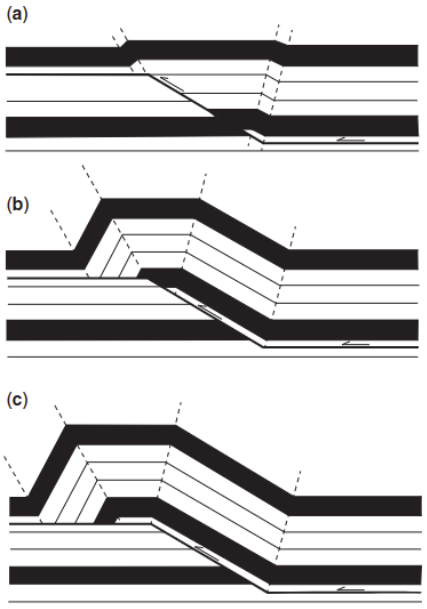

Figure 4.6: Formation of fault bend folds (J. Cosgrove, 2015).

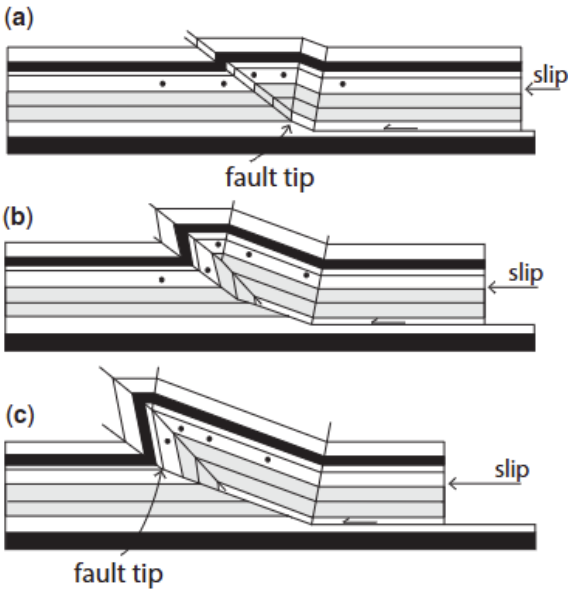

Figure 4.7: Formation of fault propagation folds (J. Cosgrove, 2015)

Fault propagation folds are formed under the same stress regime as fault bend folds, but are formed differently. Rather than detaching at the fault plane, the bedding is asymmetrically folded by the progressive growing of a fault branched in a decollement layer (Figure 4.7). It causes similar fractures as in fault bend folds, but the fracture pattern is more asymmetric with steeper fractures in the forelimb and more gentle dipping fractures in the back limb (Li et al., 2018). The fracture patterns are usually extremely chaotic (Price and Cosgrove, 1990; I. Kim et al., 2022).

5

Results

The following chapter encompasses all findings from the protocol, fracture classification, and the composite log. First, the protocol itself is presented, after which the image log interpretations are presented and the most important findings are outlined. Then, the main driving processes found in GRT-1 for the various fracture interpretations are compared. Finally, the findings of the fieldwork and the main driving processes are compared to the driving processes of GRT-1.

5.1. Protocol Implementation and Outcomes

The findings of chapter 4 have been compiled in a protocol, which presents possible pathways that can be followed based on the geologic history of the subsurface (Appendix B). The pathways of the protocol that were implemented can be found in Figure 5.1. For each expected fracture orientation, the expected relative frequency was given based on the literature.

5.1.1. Far-field Stress Fields

A series of different tectonic events impacted the fracture pattern of the URG, which were detailed in chapter 2. For each of these events, the expected fractures are the mode I fractures perpendicular to σ_3 and the mode II fractures parallel to σ_2.

5.1.2. Rittershoffen Fault

As a major fault crosses GRT-1, the depth is subdivided into five categories: the Buntsandstein protolith, the hanging wall, the fault core, the foot wall, and the crystalline basement protolith. Based on mud losses, temperature deviations, and initial well data analysis, the well intersects the fault between 2326-2366m MD. It is suggested that two of the main fluid pathways are located at the top and bottom of this interval, where 23cm and 24cm thick fractures are located, respectively. In between is the 'main fracture zone', where a significant anomaly in brine temperature was found (Vidal et al., 2017). This is therefore likely an area of significantly higher deformation and/or multiple fractures of large aperture, and has been named as the fault core.

As the top of the granite is at 2200 m(MD), the DZ of the Rittershoffen fault is initially assumed to only affect the granite. Cross sections of the area show the fault has a variable strike between N170 and N190 and a dip of 45°W (Figure 2.3; GeORG, 2017; Vidal et al., 2017). The offset of the Rittershoffen fault is estimated to be 280m. This displacement is used in the corresponding scaling law formula given in Equation 5.1.

$$T_{DZ} = \begin{cases} 10.141D^{0.2002} & \text{for foot wall} \\ 4.5652D^{0.5471} & \text{for hanging wall} \end{cases} \tag{5.1}$$

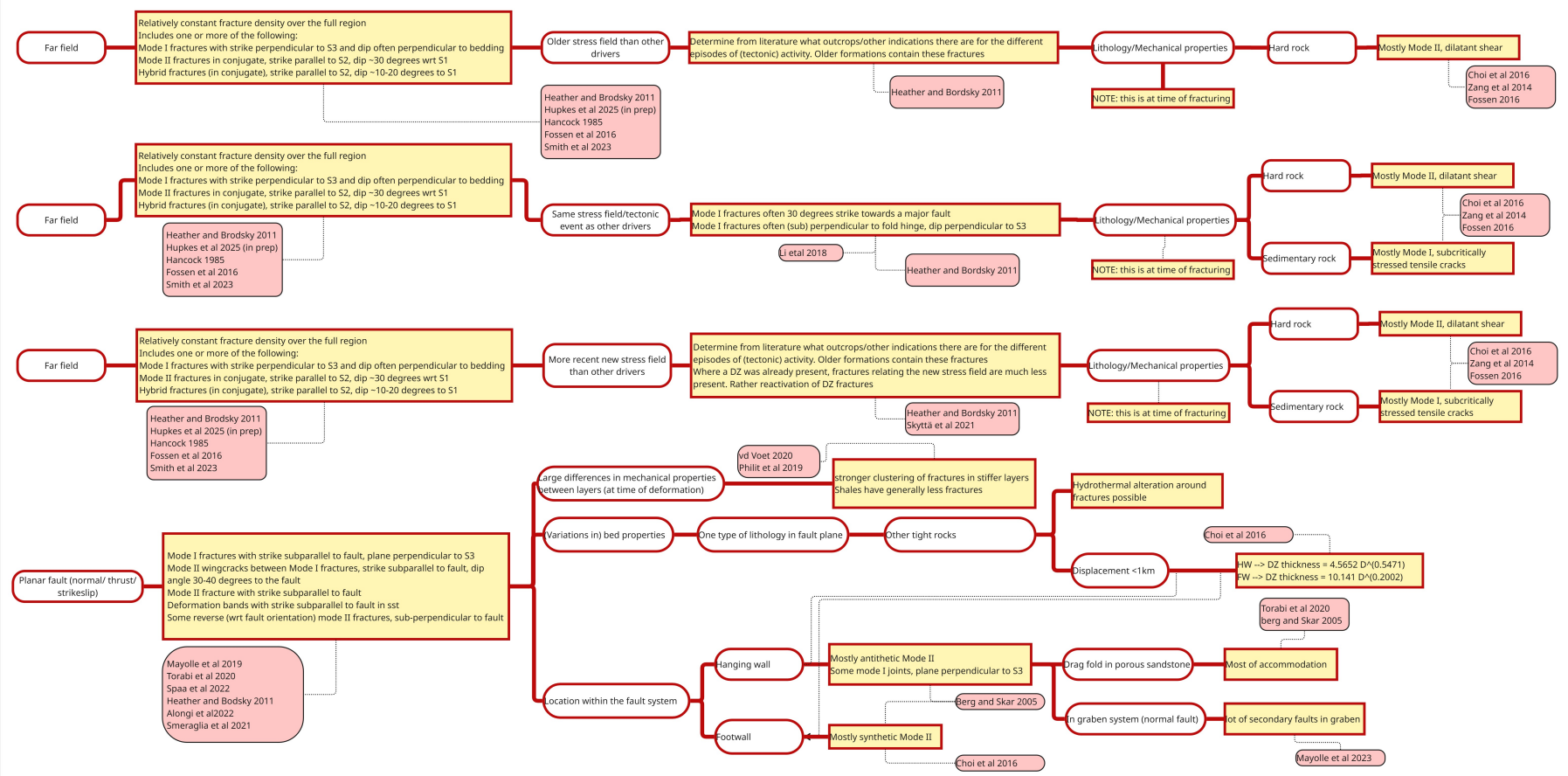

Figure 5.1: The pathways of the decision tree taken for the research area of this report. The far-field branch has been repeated multiple times for different driving events. The 'fault' branch has been followed for the Rittershoffen fault.

From this, the $T_{DZ,HW}$ is determined to be 99.6m. The $T_{DZ,FW}$ is 31.3m. Note that this is the damage zone thickness perpendicular to the fault. Therefore, the apparent damage zone thickness in GRT-1 will be $T_{DZ,HW} = 99.6/\sin(45) = 140.9$m and $T_{DZ,FW} = 31.3/\sin(45) = 44.3$m respectively. As the resolution of the prediction is meter scale, we will use 141m and 44m. 141m above the fault core results in approximately 15m of the damage zone reaching into the Buntsandstein. Note, however, as the protocol states, that the stiffer layers will accommodate most of the fractures if there are large differences in mechanical properties (Appendix B). Therefore, one would expect most fractures of the hanging wall to be located in the tight crystalline basement instead of the sandstone.

A full overview of the expected fractures derived from the protocol is given in Table A.1, illustrated in Figure 5.2, and plotted on the right-hand side of Figure 5.3.

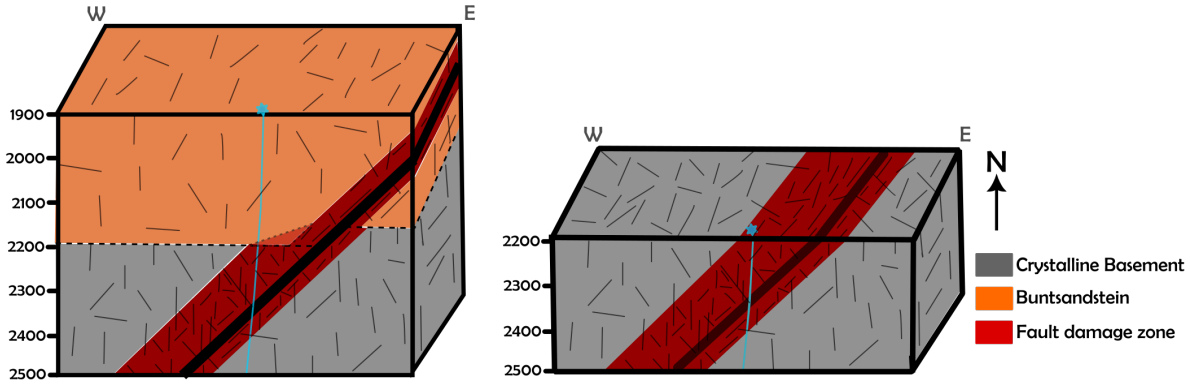

Figure 5.2: Schematic drawing of the fracture prediction in the rock around GRT-1 well. The relative intensity of fractures of different orientations and dips is represented in the drawing.

5.2. Image Log Interpretation of GRT-1

Figure 5.3 shows the poles of all the fractures picked in the fracture characterisation of the FMI and UBI image logs. Whether a fracture was mode I or II was determined largely based on the dip angle of the fracture. The majority of the orientations of the fractures in the protolith Buntsandstein and hanging wall intervals is centred around the WNW, but the dip angle is variable. The orientations of the fractures in the foot wall are similar to those found in the hanging wall, although there is a higher fraction of antithetic fractures present. The protolith of the crystalline basement shows the greatest spread in fracture orientations; the concentration of fractures is higher for orientations towards the NW, W, SSE, and E.

Note that virtually all fractures analysed during each of the interpretations were determined to be open fractures. This is a result of the thermal, chemical, and hydraulic stimulation of GRT-1 operated before logging the FMI and UBI. This stimulation implies that existing fractures are opened even if these were (partially) closed before, increasing the well injectivity by over five times (Vidal et al., 2016).

5.2.1. Clusters of Fractures

Figure 5.4 displays the cumulative fracture curves for the various interpretations. Overall, the fracture frequency is relatively constant over the complete analysed interval of the GRT-1 well. In all interpretations, the interval between 2200-2230 m(MD) encompasses the highest fracture frequency found in the well. This interval is located immediately below the top of the crystalline basement and in the hanging wall of the Rittershoffen fault. Another cluster of fractures is found between 2280-2290 m(MD), which is also located in the hanging wall. The last interval of increased fracture frequency is 1990-2000 m(MD), which is located in the protolith of the Buntsandstein succession.

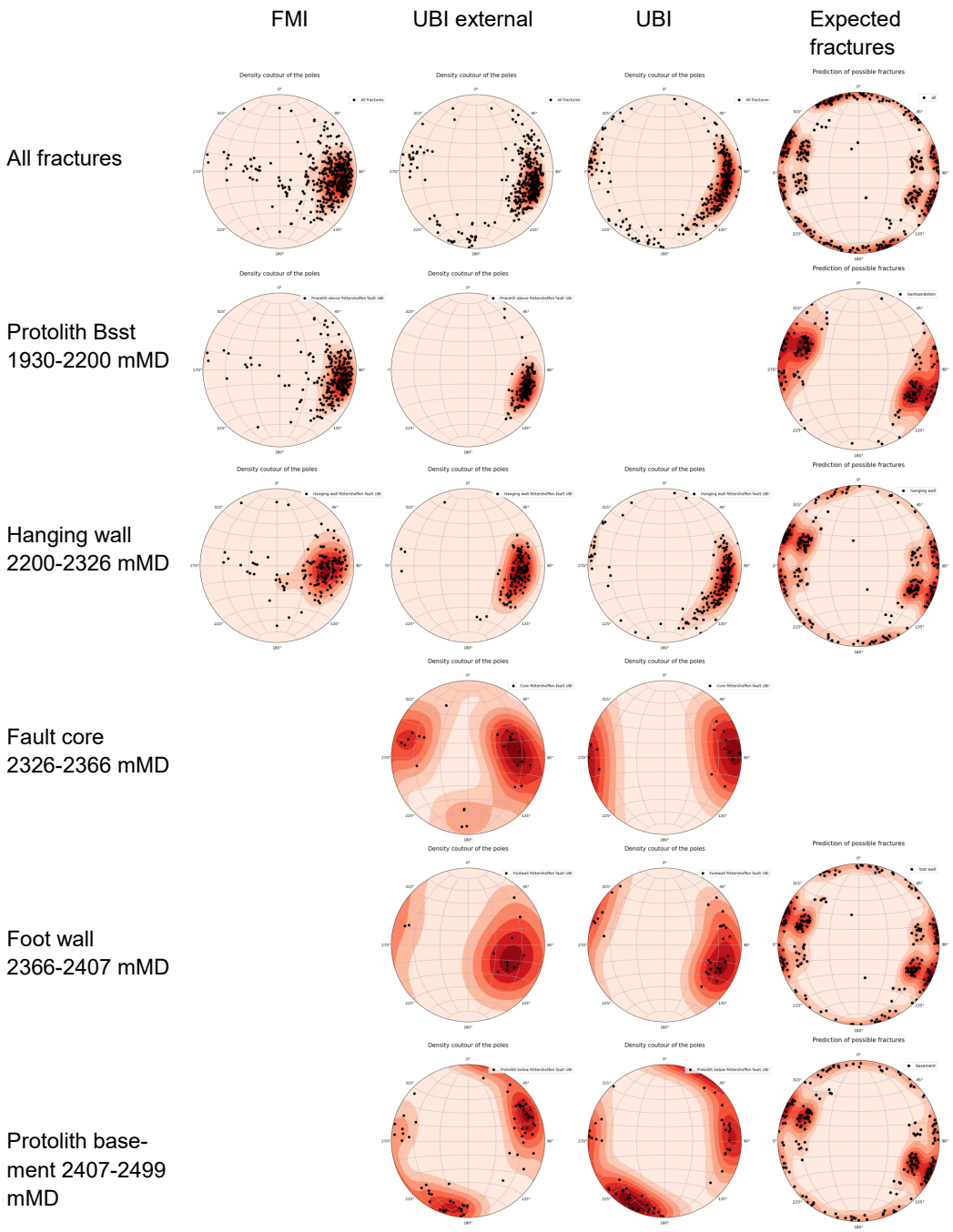

Figure 5.3: Density contour of the poles of the fractures per depth interval and interpretation. For the Buntsandstein and hanging wall of the Rittershoffen fault, you see that the dominant orientation for all interpretations is similar. The spread is wider for deeper rocks.

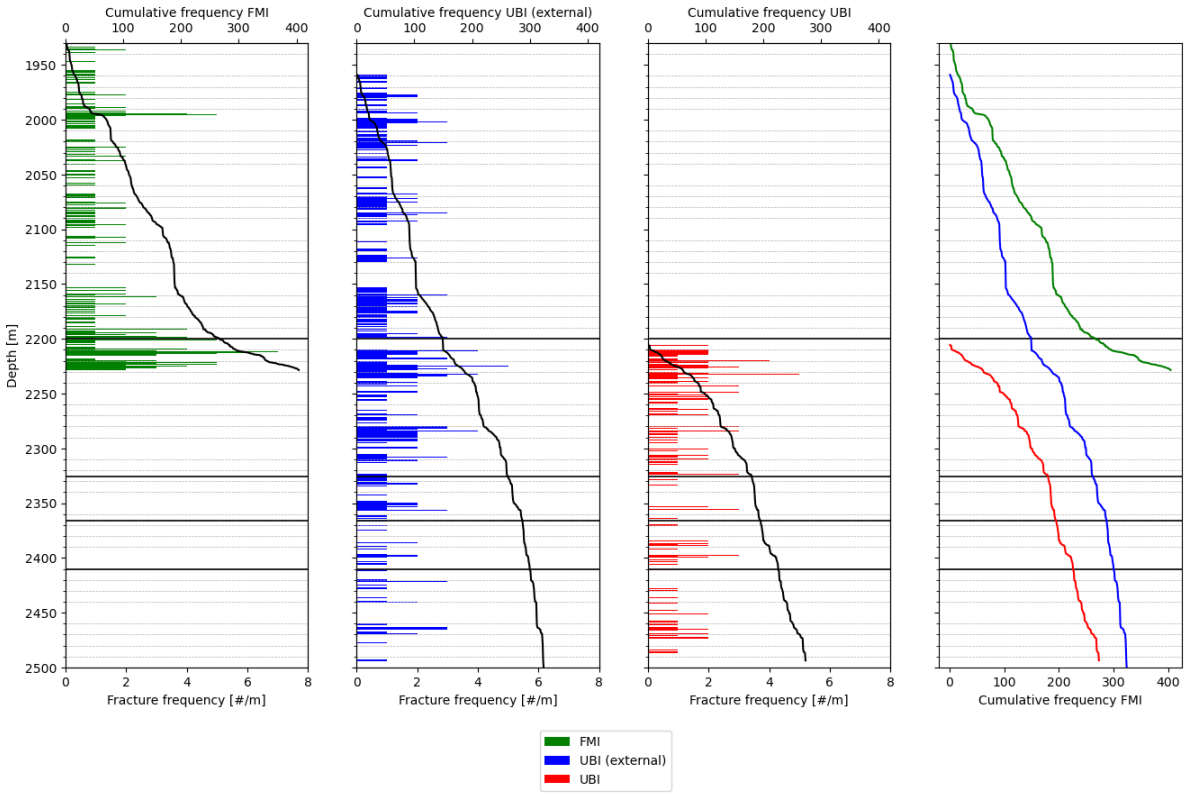

Figure 5.4: Cumulative fracture frequency of all interpretations. The fracture frequency is generally constant, but contains clusters of fractures around 1990, 2200-2230, and 2280 meters (MD).

5.2.2. Interpretations vs Expected Fractures of Protocol

As visible from the right-hand side of Figure 5.3, the orientations of the expected fractures based on the driving processes are considerably more spread than the interpretations show. The main difference for the protolith of the Buntsandstein, the hanging wall, and the foot wall compared to the expected fractures – the 'prediction' – is the symmetry of the fractures. The prediction assumed both sides of the conjugate set of fractures to form equally, while this is not the case in the GRT-1 well. Only the fractures in the foot wall show a slight increase in antithetic ESE fractures compared to the WNW fractures. Furthermore, the protocol assumes that many more and differently oriented mode I fractures have formed in the research area than are picked in GRT-1. Among all depth intervals, the protolith of the crystalline basement exhibits the lowest agreement with predicted fracture orientations.

5.2.3. Comparison Different Interpretations

Comparing the three fracture interpretations, the most prominent difference is present in the fracture intensity. Overall, more fractures are picked in the FMI log than the UBI log, and the external party picked the least amount of fractures. The interpretation of the FMI log also shows a larger spread in fracture orientations for the protolith in the Buntsandstein and the hanging wall (Table 5.1). The interpretation of the UBI log tends to have a higher dip angle than the other logs, while the external party has interpreted the least spread in fracture orientation. Nevertheless, the overall fracture patterns of all interpretations are comparable, as they originate from GRT-1.

5.3. Interpretation of Drivers and Composite Log

The different interpretations of the GRT-1 well have been classified based on the driving processes expected in the research area. Figure 5.5 shows the distribution of the fractures in the well. The composite log shows the highest concentrations of fractures in the hanging wall of the Rittershoffen fault. Generally, most fractures in the composite log are present in the granite compared to the sandstone. Figure 5.6 shows that the Miocene NW/SE compression and the Early Oligocene WNW/ESE extension

	Mean Dip	Median Dip	Std Dip	Mean Azimuth	Median Azimuth	Std Azimuth
FMI	61.70	65.09	16.13	265.28	276.33	54.36
UBI (external)	65.30	66.90	9.45	253.62	279.43	70.76
UBI	72.61	72.08	8.45	235.50	272.62	89.82
Fieldwork	80.05	83.00	9.96	219.42	252.00	102.34

Table 5.1: The mean, median, and standard deviation of each image log interpretation and the fieldwork data. The FMI has the largest spread in dip angle. The dip of the field data is the highest.

are the largest contributors to the fracture distribution. The majority of the other drivers account for only small parts of the data. In the interpretation of the FMI log, the spread of drivers is most uniform.

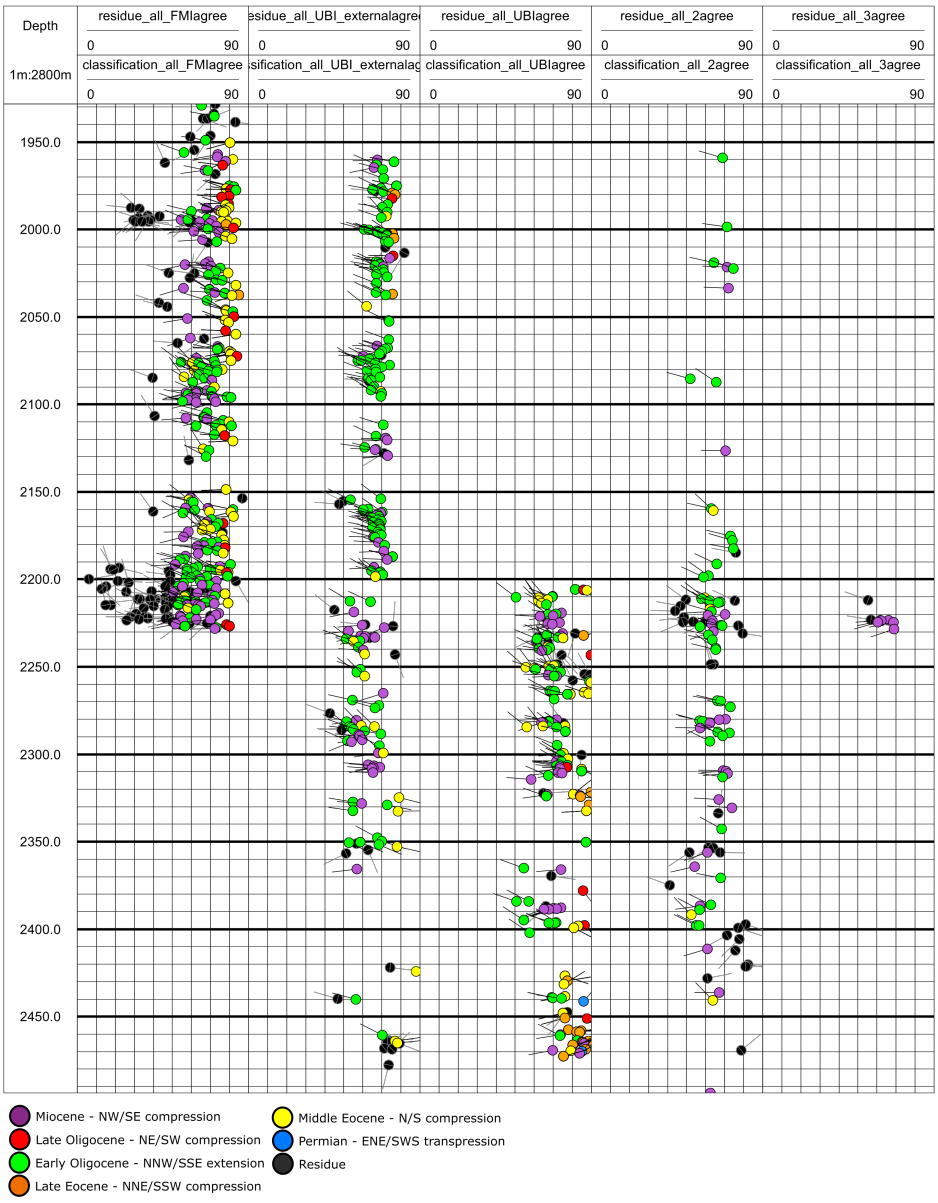

Figure 5.5: The tadpoles of the fractures picked in all interpretations and composite logs. The composite logs show most matching fractures in the granite.

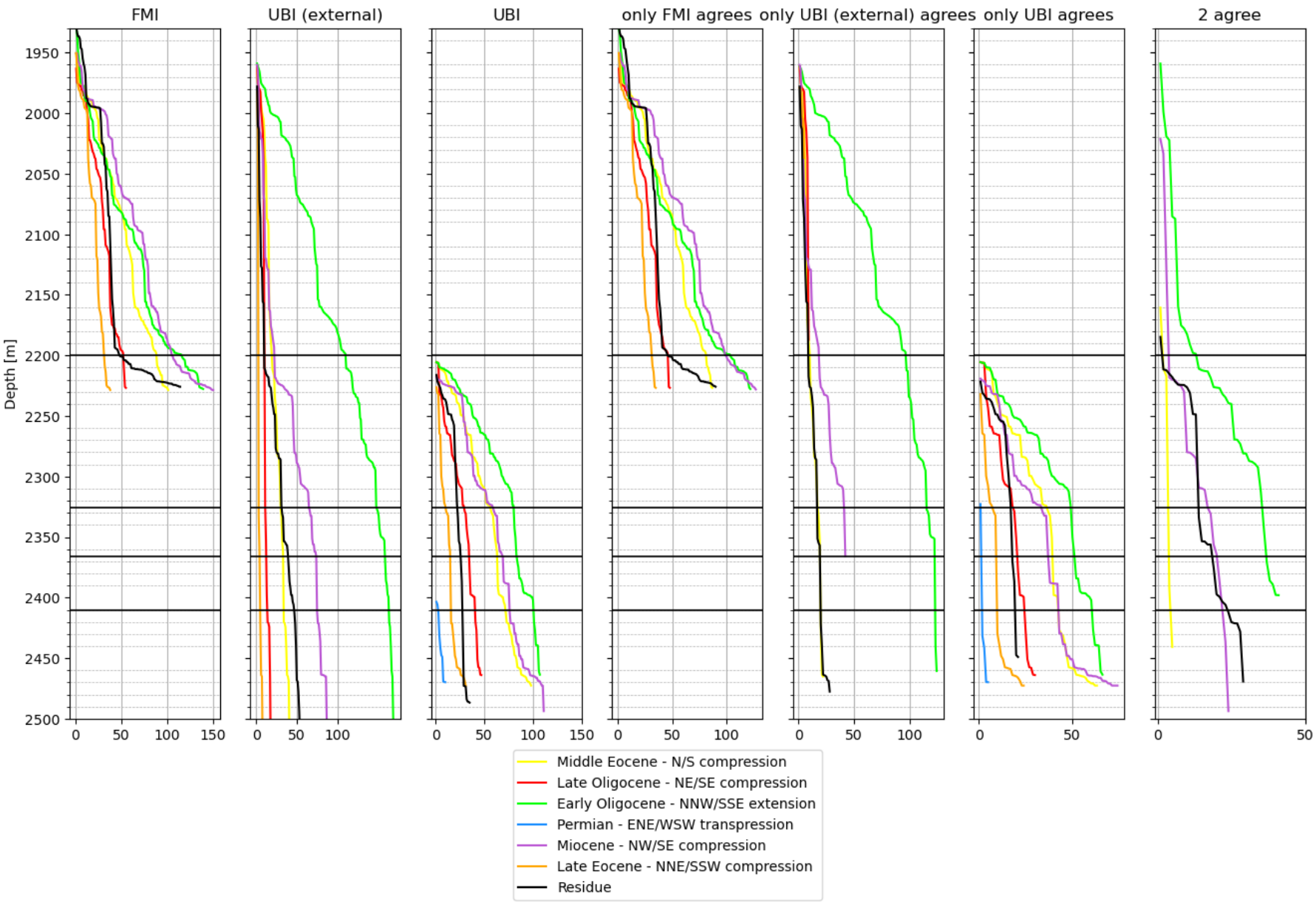

Figure 5.6: Cumulative fracture frequency in each of the different interpretations and the composite logs. The Early Oligocene and Miocene are the greatest drivers in most logs. These show the most step-wise increase in cumulative fracture frequency, indicating clusters of these fractures.

5.3.1. Permian - ENE/WSW transpression

Very few fractures were attributed to the Variscan and post-Variscan cycle. The ENE-WSW transpression was the only driving event from this geologic time period to have a sufficient amount of fractures attributed to it. The number of fractures was too small to extract trends in the dataset. The Permo-Carboniferous compression was expected to have produced 'frequent' fractures, but this event was not linked to any fractures in the crystalline basement. The same goes for the late Variscan dextral strike-slip event.

5.3.2. Middle Eocene - N/S compression

Fractures linked to the Middle Eocene N/S compression show a relatively uniform distribution throughout the various depth intervals. The composite log contains fewer fractures derived from this driver.

5.3.3. Late Eocene - NNE/SSW compression

The protolith of the Buntsandstein and the hanging wall and foot wall of the Rittershoffen fault contain very few to no fractures related to this event. However, the protolith of the crystalline basement has a larger share in this fracture orientation (Figure 5.7A).

5.3.4. Early Oligocene - WNW/ESE extension

The extension phase accounts for the largest share of the fracture distribution. However, there is also the largest variability between the depth intervals and interpretations. As seen in Figure 5.7B, in the protolith of the Buntsandstein, the externally interpreted UBI log shows 64% of the fractures in the range of orientations related to the extension phase. However, the interpretation of the FMI log shows only 26.2% of the fracture can be attributed to this event. In contrast, the composite log accounts for 72.2% of this orientation of fractures. Most fractures in the hanging wall and foot wall of the composite log can also be linked to the Early Oligocene extension (Figure 5.7C). Figure 5.6 shows that the fractures attributed to the Early Oligocene extension are present in short, clustered intervals rather than present uniformly throughout all depth intervals.

It is noted that the fracture orientations of the Late Eocene NNE/SSW compression overlap with the fractures related to the Early Oligocene. The same is true for the sinistral strike-slip Rhenish shear zones of the Permo-Carboniferous time period. Furthermore, the fractures of the Early Oligocene are possibly reactivated by Late Oligocene dextral reactivation of the graben and Miocene sinistral reactivation of the graben.

5.3.5. Late Oligocene - NE/SW compression

The presence of fractures related to this driving process is fairly constant in the protolith of the Buntsandstein, with a mean of 8.7% and a standard deviation of 2.3%. The interpretation of the UBI log contains the highest fraction of these fractures compared to the FMI and external UBI interpretations. Furthermore, the composite log shows no fractures attributed to the Late Oligocene compression. Figure 5.6 indicates a relatively constant frequency of the fractures over the analysed depth interval of the GRT-1 well.

5.3.6. Miocene - NW/SE compression

The fractures related to the Miocene NW/SE compression are present in clusters. Nevertheless, the fraction of these fractures is consistent throughout all interpretations and depth intervals. The mean fraction is 24.7% with a standard deviation of 7.9%. The hanging wall contains the highest fraction of these fractures. This is also the only driving process found in the composite log where all three interpretations agree (the hanging wall, Figure 5.7D). The composite log where three interpretations agree is excluded from any statistical analysis, as the dataset is too small to be taken into account (eight fractures in total). The fractures related to the Miocene compression were often also related to the Rittershoffen fault. It is hypothesized that the Rittershoffen fault is produced by the Miocene compressional regime, causing releasing bends between the border faults of the URG (Schumacher, 2002). Therefore, the Rittershoffen fault is categorized as another driving process of these fractures.

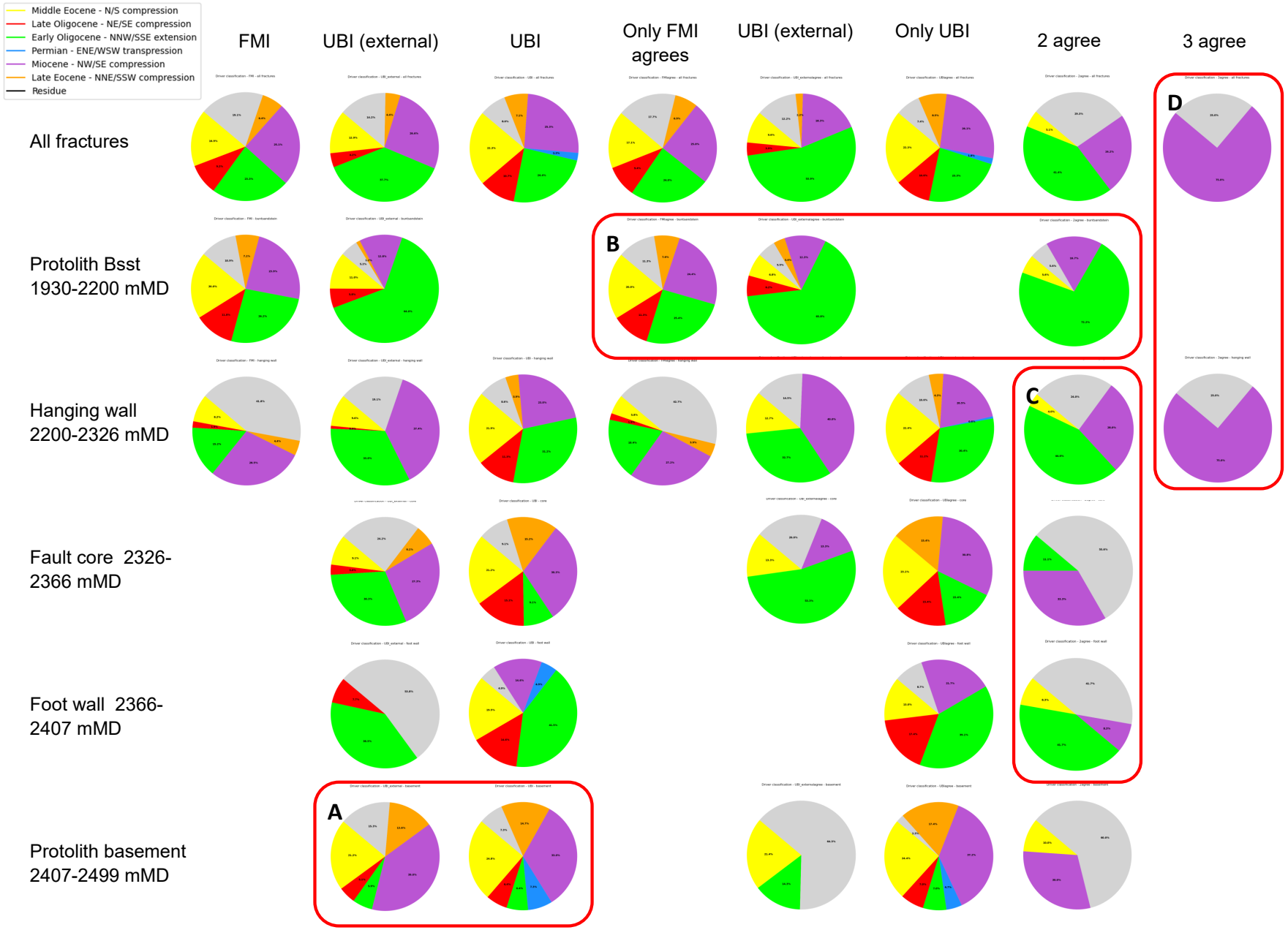

Figure 5.7: Percentage of each driver per depth interval and type of data interpretation. A: The protolith of the crystalline basement has the largest relative share of the Late Eocene driving process. B: The Early Oligocene extension has a variable fraction of fractures in the different interpretations. C: The hanging wall and foot wall in the composite log of two agreements are dominated by the Early Oligocene extension. D: The only driver found in the composite log of three agreements is fractures related to the Miocene compression.

5.3.7. Residue

Residual fractures are defined as fractures that do not fit in one of the driving processes above, or that are not categorized to a driving process where more than five fractures are attributed. The residual fractures are primarily present in short intervals of higher fracture concentration, which is the reason why the hanging wall of the interpretation of the FMI log contains a high fraction of residual fractures (41.8%). The interpretation of the UBI log contains overall 8.0% of residual fractures, which is the least of all interpretations. In the composite log, the protolith of the Buntsandstein only consists of 5.6% residual fractures, while this fraction increases to up to 55.6% for deeper depth intervals. Figure 5.8 shows the residual fractures of the various interpretations. The fractures are very spread out for all interpretations. FMI interpretation accounts for 52.9% of all residual fractures, the mean of the dip is 45.74°, and the standard deviation is 17.37°.

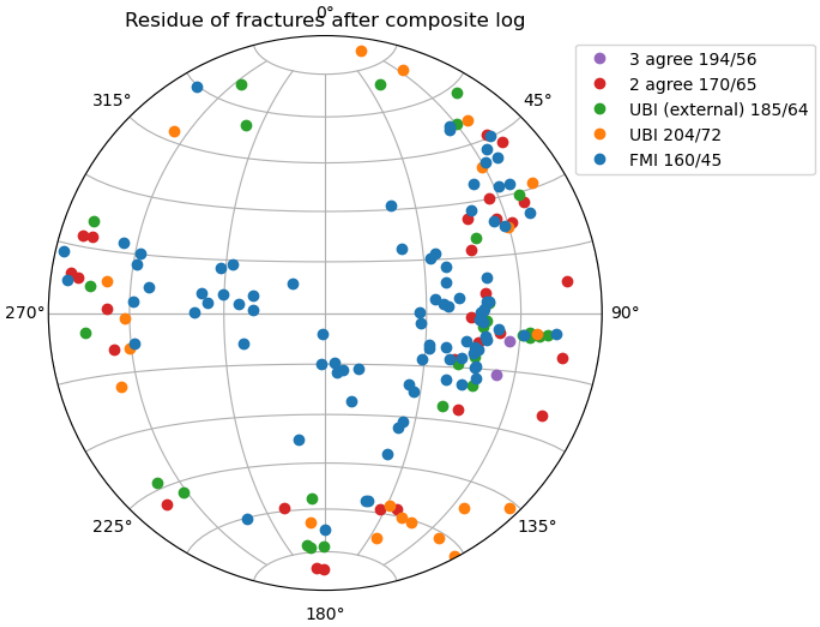

Figure 5.8: Distribution of the residue fractures after classification of the driving processes for each interpretation.

5.4. Protocol in Fieldwork - 3D

5.4.1. Crystalline Basement

The crystalline basement was only investigated through cores of the EPS-1 well. Generally, the fractures were cemented or had very little aperture. The fractures in EPS-1 were often difficult to distinguish because the colours of the granite and fracture filling were similar. However, large fractures were easily recognized: Figure 5.9 shows mode II shear fractures in the basement. The fractures generally appeared to be clustered rather than have a constant fracture frequency over the full log. Such fractures have likely been opened by the stimulation in the GRT-1 well (Vidal et al., 2016). Very small fractures (<10-scale in length) were also abundantly present, though these typically have limited impact on reservoir-scale fluid flow compared to fractures with larger apertures.

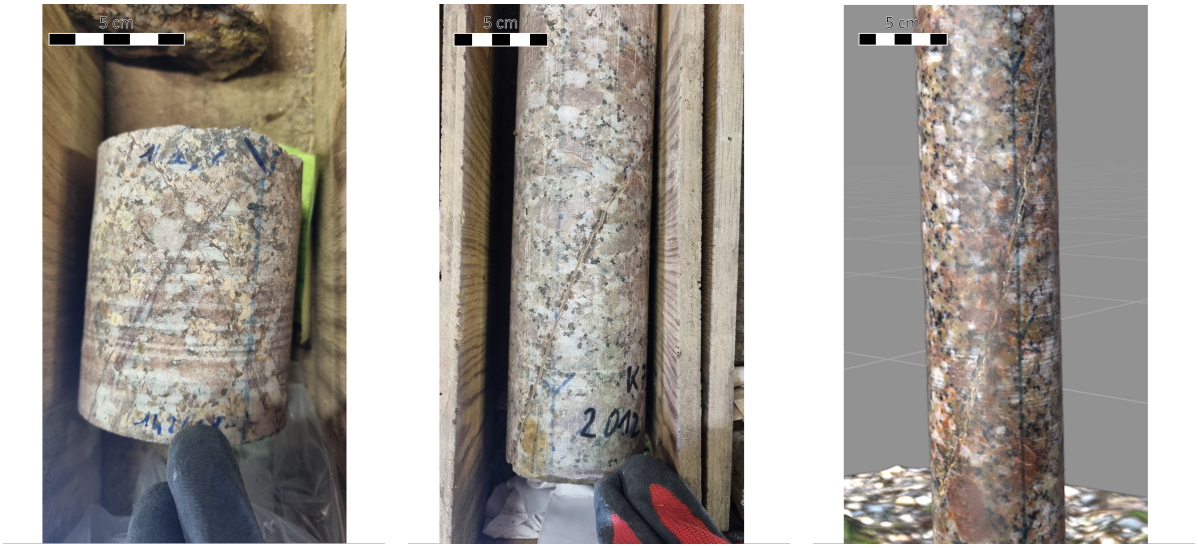

Figure 5.9: Examples of different types of fractures present in the crystalline basement (not stimulated).

5.4.2. Buntsandstein

The fractures in the Buntsandstein cores of EPS-1 appear similar to the fractures in the crystalline basement: (partially) filled, generally little aperture, and short intervals of higher fracture frequency are abundant (Figure A.4). Some fractures show small (<2cm) displacement along the fracture plane, although no apparent displacement was detected for very steep fractures (>75°).

The outcrops of the Buntsandstein succession on the shoulder of the URG have also shown the presence of intervals of increased fracture frequency (Figure 5.10), but the outcrops did not contain high amounts of fractures overall. The mean dip angle is significantly higher than in all of the image log interpretations (Table 5.1). Furthermore, the fracture distribution in the outcrops shows much more symmetry than the GRT-1 well (Figure 5.11).

The same driving process classification has been performed on the fractures measured in the outcrop as for the fractures in the GRT-1 well (Figure 5.12). Only 5.6% of the fractures in the outcrops are linked to the Early Oligocene extension, whereas this driving process represents 26.2% in protolith of the Buntsandstein in GRT-1 and 72.2% in the composite log. All other drivers account for a similar fraction of the fractures in the outcrops as in the FMI log. However, the composite log does not contain any fractures related to the Late Oligocene and Late Eocene compression, and underestimates the relative amount of fractures caused by the Middle Eocene compression.

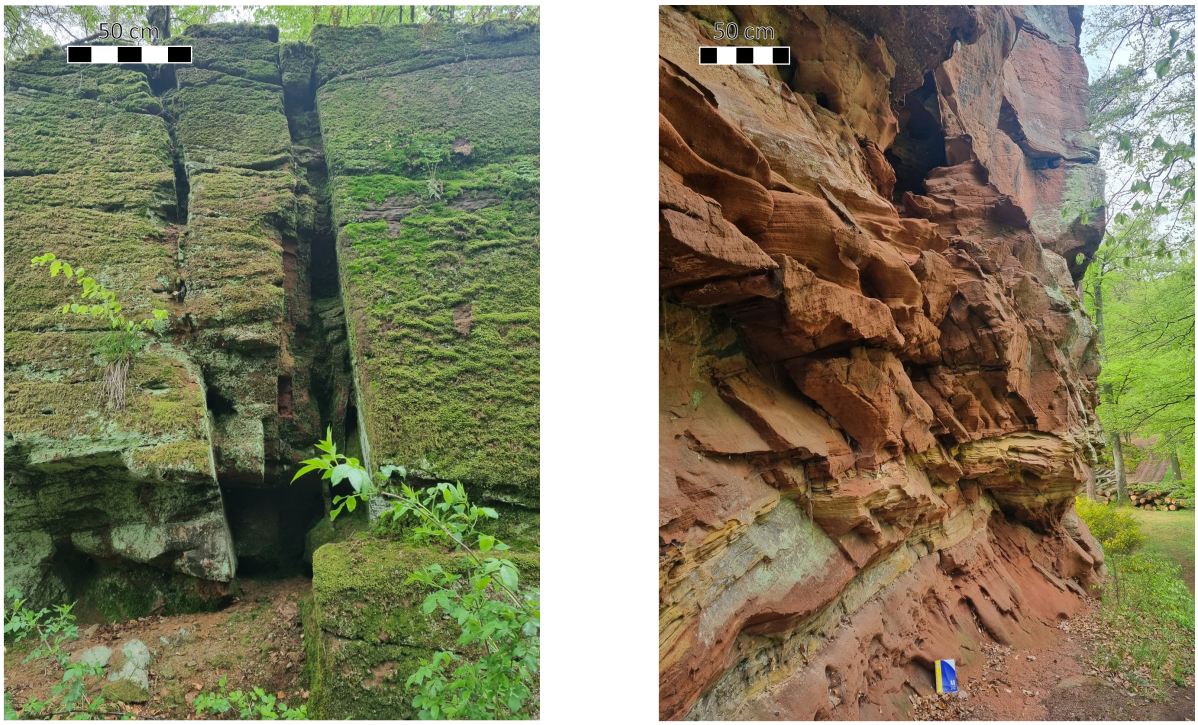

Figure 5.10: Fracture clusters at the Falkenstein and Helphenstein Ruin outcrop.

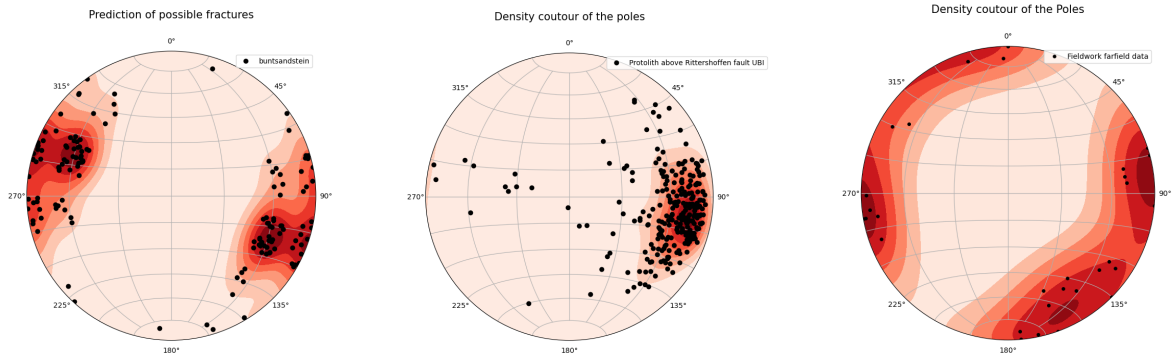

Figure 5.11: Fracture distribution of protolith of the Buntsandstein. Left: expected fracture distribution. Centre: picked fracture distribution in the FMI log. Right: measured fracture in outcrops.

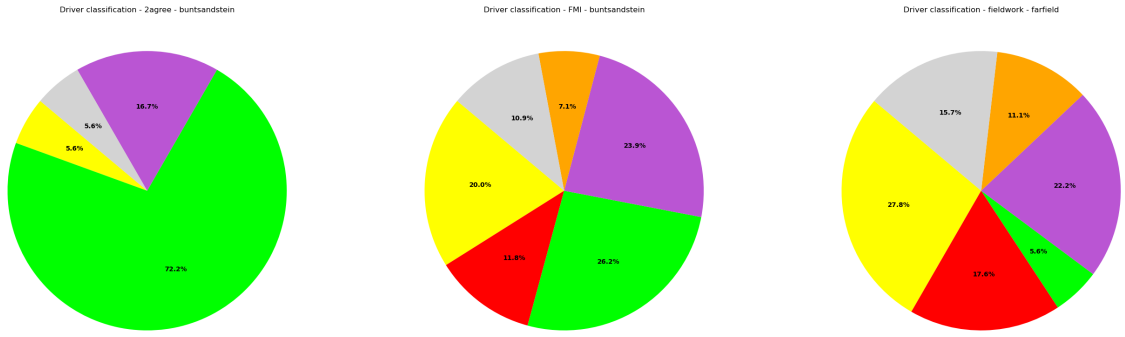

Figure 5.12: Distribution of the various driving processes of protolith of the Buntsandstein. Left: expected fracture distribution. Centre: picked fracture distribution in the FMI log. Right: measured fracture in outcrops. The same colour legend as before has been applied.

6

Discussion

The discussion has been subdivided into four major parts. First, the interpretation of the fracture data of GRT-1 is discussed. Then, the effectiveness of the protocol is analysed, followed by a summarizing statement on the practical value of the protocol. Lastly, the limitations and recommendations are outlined.

6.1. Interpretation of GRT-1, Drivers, and Composite Log

6.1.1. Main Driving Processes

The most common fracture driving processes in the GRT-1 well are the Early Oligocene WNW/ESE extension phase and the Miocene NW/SE compression phase. The composite log where two interpretations align reinforces the hypothesis that the Early Oligocene extension is a key contributor to the fracture distribution in this research area. The Miocene compressional phase is consistently observed across all depth intervals, though these tend to be clustered in pockets. This is the only driving process for which all three interpretations have an agreement.

From the protocol, the Early Oligocene extension phase was expected to be the most common throughout the interval. However, the fractures produced by the Early Oligocene extension were present mostly in the Buntsandstein and the damage zone of the Rittershoffen fault, but were sparse in the protolith of the crystalline basement. In contrast, the fractures linked to the Miocene compression and by extension the Rittershoffen fault are more consistently present throughout the Buntsandstein and crystalline basement instead of being focused in the DZ intervals.

A possible explanation for this is that the size of the foot wall DZ is overestimated. Damage zone thickness scaling laws have been highly debated (chapter 4) and are therefore notoriously difficult to predict. Additionally, the tectonic events are acting upon the entire research area. An increase in the Miocene fractures is expected closer to the Rittershoffen fault, but these were likely formed over the entire section. Furthermore, the fault core defined here is in fact the main fracture zone of the Rittershoffen fault, and the depth of the true fault core is debated. In turn, the DZ thicknesses might be skewed as well. Lastly, it is suggested that the Rittershoffen fault was formed as a releasing bend during the Miocene sinistral strike-slip reactivation of the URG. However, this is highly speculative. A great source of uncertainty is the exact tectonic event that has created the Rittershoffen fault. If this was formed during the Early Oligocene extension, the distribution of the classified fractures would make more sense. However, the principal stress orientation fits best with the Miocene sinistral reactivation of the graben. It is recommended to have a solid understanding of the tectonic event behind drivers such as master faults in order to implement the protocol.

6.1.2. Other Driving Processes

Most driving processes that are classified are present relatively uniformly over all depth intervals. Notably, only the fractures related to the Early Oligocene and the Miocene are present in clusters, which are also the two most commonly classified driving forces. This gives rise to the speculation that the more fractures a driver produces, the more likely small clusters of fractures are to form.

The fracture distribution in the protolith of the crystalline basement is significantly different from that

of the Buntsandstein, which confirms that the basement has indeed had a more extensive tectonic history than the Buntsandstein. From the driving process classification, the driving forces that were only present in the crystalline basement were the Permian ENE/SWS transpression and the Permo-Carboniferous compression. The lack of other driving processes is likely due to possible reactivation or sealing of fractures created before the Triassic period.

Unsurprisingly, two of the most recent major tectonic events account for the most prominent and consistently observable fracture sets. Because these events occurred relatively recently in geological terms, these fractures are less likely to have been sealed or obscured, making them more readily detectable. This highlights that the protocol is more effective at classifying fractures caused by more recent tectonic activity, while its sensitivity to older, less well-preserved fracture systems appears more limited.

6.1.3. Variations in Interpretations

Although the differences between the various image logs are not the main focus of this report, these are important to note to adequately compare the similarities and differences between the interpretations. Foremost, comparing the datasets using a composite log is extremely sensitive to differences in depth, azimuth, and dip angle. Therefore, strict care must be taken in the setup and processing of the image logs before the fracture characterisation even begins.

The interpretation of the FMI log contains the most fractures compared to both interpretations of the UBI log. This is likely because of the difference in resolution of the image logs; the vertical resolution of FMI logs is four times higher than the UBI log. Besides this, the difference between interpreters, especially between the externally interpreted and the new interpretations, can be explained by subjective bias. The level of experience, thought processes during the interpretation, and even personality might have caused these differences.

The external interpretation generally contained fewer fractures and was much less widely spread, while the interpretation of the FMI data shows a larger spread and intensity of fracturing. Even though the higher vertical resolution of the FMI log allows for thinner fractures to be picked, the separate image columns make tracing the fractures more difficult (Figure 3.2). This might give rise to more fractures with a wider spread of orientations and dip angles.

6.1.4. Comparison GRT-1 and Fieldwork

Even though the fracture distribution of the protolith of the Buntsandstein looks quite different for the FMI interpretation and the fractures measured in outcrops, the classification of the fractures is similar. The largest difference in fracture driving processes is the Early Oligocene. In the field, very few fractures could be attributed to this driver, while this is the largest driving force of the interpretation of the FMI log. The Early Oligocene extension is the tectonic event that created the URG. Since the outcrops are on the shoulder of the graben and the reservoir inside the graben, it is logical that this driving force has resulted in a different fracture pattern in these respective areas. Some of the less prominent driving forces are also not found in the fieldwork. This can have various reasons. The tectonic history can be slightly different at Rittershoffen compared to the outcrop locations, or possibly the outcrops have not included five or more of these fractures. Additional research is needed to draw adequate conclusions from this.

Furthermore, the 3D overview of the outcrops has given additional information on the extrapolation of the data gathered in the GRT-1 well. In the interpretation of the BHI logs, as well as in the field measurements and the EPS-1 cores, clusters of fractures were present for the Buntsandstein formations. Therefore, this type of feature could be incorporated into (3D) fracture network models. The fractures analysed in the EPS-1 cores also suggest these clusters might be present in the crystalline basement.

Mode I fractures were likely underestimated in the GRT-1 well. Mode I fractures are often vertical, and the near-vertical well would not have crossed most of these fractures. In the field, very steep (>75°) fractures were found much more frequently throughout the outcrops. The orientation of the well must be taken into consideration when applying the protocol.

6.2. Effectiveness of Protocol

6.2.1. Overlap of Driving Processes

In all interpretations, especially in the Buntsandstein and hanging wall depth intervals, the fracture orientations are centred towards the NNW. It is intuitive to assume these fractures are produced by one fracture driver. However, the classification done in this research showed multiple drivers can be linked to this, partly overlapping. It is therefore highly recommended to investigate the different ranges of azimuth and dip angle related to each driving process.

Many driving processes that were rarely expected according to the protocol are indeed not classified for more than five fractures per interpretation. However, some fractures that were expected rarely have been classified throughout the interpretations, such as the fractures linked to the Late Eocene. In this case, it is likely because the orientations are closely related to the Early Oligocene or other drivers, but differ by 2.5°. This highlights the idea to experiment with the range of fracture orientations allowed per driver. Even though an over-estimation of the number of fractures driving processes does not impact the interpretations negatively, it does diminish the effect of utilizing the protocol to justify fracture patterns in data interpretations.

Two driving forces were expected to have produced 'common' fractures, yet these have not been linked to many fractures separately: the Late Variscan compression and the Permo-Carboniferous compression. It has been postulated that the fractures produced by the latter have been reactivated during the Early Oligocene extension. As both the Late Variscan and the Permo-Carboniferous compression are older fracture drivers, it is expected that these have been overprinted, sealed, or reactivated and are therefore not visible in the image logs.

6.2.2. Unclassified Fractures

There is a large spread of orientations of the residual fractures. A slightly higher concentration of fractures is present between 045-070N and dip angle 60-70, which could mean that the protocol has not been followed for one or more driving processes. However, this is a low concentration of fractures.

The hanging wall hosts the largest intervals of higher concentrations of fractures, which is expected in a damage zone. Almost all residual fractures were located in these clusters, specifically in the FMI interpretation. This indicates that these 'clusters' give rise to a greater variability of fracture orientations than is originally predicted by the protocol. This would be important to keep in mind when analysing BHI logs with very frequent fracture clusters or generally high concentrations of fractures.

6.3. Practical Value of the Protocol

It should be noted that the protocol will never give a perfect prediction of the expected fractures in any outcrop or well. Apart from the inherent heterogeneity of the subsurface, the tectonic events are not isolated or instant events. This takes millions of years and is a dynamic process, which can make these predictions very difficult to make. However, the protocol provides a solid guideline for fracture interpretation, which makes discussions between interpreters more streamlined. The added value of utilizing this protocol for not only image log interpretation, but arguably for outcrop interpretation as well, is three-fold.

Structuring Interpretations

Fracture characterisation is vulnerable to subjective bias, for example, in terms of orientations, dip angle, and intensity. The interpretations of the FMI and UBI logs of GRT-1 and the fractures measured in the field have shown this variability in fracture attributes. However, the protocol and classification forces the interpreter to think about the interpretation before, during, and after picking the fractures. Multiple pathways of possible fracture driving processes are proposed, where the interpreter has to manually choose and investigate whether these are present in the research area or not. Presenting multiple hypotheses of what could be present in the research area is a highly recommended tactic to reduce availability bias (chapter 2). This results in a structured, substantiated fracture characterisation.

Justify and Support Interpretations

The protocol allows for a justification for the selection of the fractures that have been classified. The underlying thought process of picking the fractures is documented and can therefore be discussed and

debated with other interpretations more constructively. This discussion will give rise to the most reliable fracture characterisation of the discussed area.

Effective Integration into 3D DFN Modelling

Discrete Fracture Network (DFN) modelling is of key importance when analysing the secondary permeability of a research area. Populating this model is therefore essential. The protocol and classification framework proposed in this study provide a supported parametrization for the DFN model by providing estimates of expected fracture orientations, dip, intensity, clustering, and, to some extent, spatial variability. Integration of image logs and analogue outcrops will be essential in this parametrization.

6.4. Limitations and Recommendations

6.4.1. Development of the Protocol

Although the protocol that is developed encompasses many different branches of fracture driving processes and circumstances, relatively few of the pathways are tested. Therefore, the main recommendation for future research is testing, expanding, and constraining the protocol. This will standardize the protocol further and improve the overall fracture predictions resulting from the analysis.

The advantage of a standardized protocol is that it is widely applicable in different geological settings. However, it is imperative to maintain an open and adaptable approach when applying the protocol to new research areas, as each geological setting presents unique characteristics that may influence fracture patterns. For GRT-1, this includes the presence of fracture clusters, the preferred fracture orientation of a conjugate fracture set, and the impact of well stimulation. Such unique characteristics should be taken into account to refine and personalize the expected fracture pattern.

As suggested before, the range of tolerance for the azimuth and dip angle for each driving event can be explored. The fracture distribution of GRT-1 appears to be caused by one driving event at first glance, though the fracture classification based on the protocol shows multiple drivers have contributed to this spread. However, wider ranges of the azimuth and dip angle might show that there is one dominant driver responsible for the fracture distribution, or it will confirm that the fractures are produced by different driving processes. Furthermore, wider ranges in the dip angle specifically will reduce the amount of unclassified fractures in the clustered areas. As the subsurface is generally heterogeneous, it is not recommended to decrease the ranges for the azimuth and dip angle further.

The protocol can still be improved in terms of the expected frequency and confidence of the fractures. The expected frequency was investigated and noted manually in this research based on the literature and the suggested frequency in the protocol. While this approach is solid, the suggested frequency should be more detailed and clearly stated in the protocol. Currently, confidence levels are not assigned to individual fractures. Typically, confidence is determined based on the visibility of the sinusoid in the image logs. However, evaluating confidence based on how well a fracture aligns with the expected orientation patterns could offer additional insight into the reliability of individual picks, potentially reducing the immediate dependence on a composite log for validation.

From the analysis done on GRT-1, it has become clear that the orientation of the well needs to be taken into account when noting the expected fractures; if the well is near-vertical, significantly fewer mode I fractures are expected to be present. However, even though the well will rarely intersect the fractures, these are important to note for the 3D extrapolation of the fracture network.

6.4.2. Development of the Composite Log

The greatest limitation regarding the composite log was integrating the different types of image logs. The UBI and FMI files had been pre-processed differently, which resulted in a depth offset between the two image logs. This had to be manually corrected, but was likely not done in detail enough for the composite log processing, which requires cm-scale accuracy. Therefore, a detailed account of the (pre)processing of the image logs is recommended to avoid these issues. It is expected that more fractures will be in agreement when this reassessment is done. Implicitly, this means that some fractures in agreement currently are likely not the same fracture. As such, the composite warrants a cautious interpretation.

Furthermore, FMI image logs consist of eight separate image columns, with interpolation necessary to

generate a continuous fracture pick. However, minor offsets between the columns introduced inconsistencies that made accurate interpolation more challenging. Based on this, an offset log can be created, where an offset higher than a certain threshold indicates that this depth interval was challenging to assess. Additionally, an Image Complexity Map (ICM) can be generated in WellCAD that shows how complex the image log is based on the contrast between the fractures and the rock. Similarly, the composite log of this study shows the agreement between different interpretations, and thus which depth intervals contain fractures that were more easily picked than others. In future research, these three logs can be compared to see if the offset log and ICM can predict, to some degree, which fractures will be more reliable without the need to compare multiple interpretations of the same well. This will save time and thus costs in interpreting the data.

As stated in earlier sections, it is highly recommended to explore the range of tolerance to create the composite log. The azimuth and dip angle are now set at a range of ±15° but possibly a smaller range is preferred to ensure that the composite fractures are indeed the same in both logs.

7

Conclusion

This research aimed to analyse the effect of a standardized protocol for linking fractures to driving geological processes on the justification of the FMI and UBI log interpretations of the GRT-1 well in Rittershoffen, France.

The protocol offers a structured guideline for fracture characterisation, reducing availability bias. Communication between interpreters will be more constructive by documenting the reasoning behind fracture picks. The composite log, while sensitive to processing inconsistencies, provided a useful validation for correlating fractures across different datasets, reinforcing the protocol's value in identifying reliable fracture patterns. The protocol supports effective 3D DFN modelling by constraining the expected fracture network based on both image logs and field data. Note, however, that the effectiveness of the protocol is partially limited by, e.g., the resolution differences in the image logs that are compared, and the uncertainty of the definition of fracture driving processes, emphasizing the need for further investigation.

The majority of fractures picked in both the fieldwork and the FMI and UBI image logs have been linked to one or more fracture driving processes. Using the protocol, the main fracture driving processes in the research area have been determined to be the Early Oligocene ENE/SWS extension and the Miocene NW/SE compression. The Rittershoffen fault has been assigned to the same fractures as the Miocene NW/SE compression, alluding to the fact that the Rittershoffen fault might have been produced or reactivated in the Miocene. Furthermore, many fractures assigned to fracture drivers from the Paleozoic have been reactivated or obscured by more recent, pronounced driving processes. Conversely, many expected fracture drivers were not linked to any of the interpreted fractures.

It is concluded that even though the protocol has proved very effective in structuring and justifying the interpretation of both image logs and outcrops in many different geological settings, thorough testing, constraining, and expanding of different pathways will further improve the standardized protocol.

References

Ahorner, L. (1975). Present-day stress field and seismotectonic block movements along major fault zones in central europe. In *Developments in geotectonics* (pp. 233–249, Vol. 9). Elsevier.

Alcalde, J., & Bond, C. E. (2022). Subjective uncertainty and biases: The impact on seismic data interpretation. In *Interpreting subsurface seismic data* (pp. 103–123). Elsevier.

Alongi, T., Brodsky, E. E., Kluesner, J., & Brothers, D. (2022). Using active source seismology to image the palos verdes fault damage zone as a function of distance, depth, and geology. *Earth and Planetary Science Letters*, *600*, 117871.

Andrews, B. J., Mildon, Z. K., Jackson, C. A., & Bond, C. E. (2024). Quantifying fault interpretation uncertainties and their impact on fault seal and seismic hazard analysis. *Journal of Structural Geology*, *184*, 105158.

Andrews, B. J., Roberts, J. J., Shipton, Z. K., Bigi, S., Tartarello, M. C., & Johnson, G. (2019). How do we see fractures? quantifying subjective bias in fracture data collection. *Solid Earth*, *10*(2), 487–516.

Baillieux, P., Schill, E., Edel, J.-B., & Mauri, G. (2013). Localization of temperature anomalies in the upper rhine graben: Insights from geophysics and neotectonic activity. *International Geology Review*, *55*(14), 1744–1762.

Bally, A., Bernoulli, D., Davis, G., & Montadert, L. (1981). In listric normal faults failles normales listriques. *Proceeding 26th international geological congress; Geology of Continental Margins Symposium: Paris*, 7–17.

Balsamo, F., La Bruna, V., Bezerra, F. H., Dall'Aglio, M., Bagni, F. L., Silveira Jr, L. G., & Aires, A. S. (2023). Mechanical stratigraphy controls fracture pattern and karst epigenic dissolution in folded cretaceous carbonates in semiarid brazil. *Marine and Petroleum Geology*, *155*, 106409.

Bárdossy, G., & Fodor, J. (2001). Traditional and new ways to handle uncertainty in geology. *Natural Resources Research*, *10*, 179–187.

Bauer, J. F., Krumbholz, M., Meier, S., & Tanner, D. C. (2017). Predictability of properties of a fractured geothermal reservoir: The opportunities and limitations of an outcrop analogue study. *Geothermal Energy*, *5*, 1–27.

Baujard, C., Genter, A., Dalmais, E., Maurer, V., Hehn, R., Rosillette, R., Vidal, J., & Schmittbuhl, J. (2017). Hydrothermal characterization of wells grt-1 and grt-2 in rittershoffen, france: Implications on the understanding of natural flow systems in the rhine graben. *Geothermics*, *65*, 255–268.

Bazalgette, L., Petit, J.-P., Amrhar, M., & Ouanaimi, H. (2010). Aspects and origins of fractured dip-domain boundaries in folded carbonate rocks. *Journal of Structural Geology*, *32*(4), 523–536.

Berg, S. S., & Skar, T. (2005). Controls on damage zone asymmetry of a normal fault zone: Outcrop analyses of a segment of the moab fault, se utah. *Journal of Structural Geology*, *27*(10), 1803–1822.

Bertani, R. (2009). Geothermal energy: An overview on resources and potential. *Proceedings of the international conference on national development of geothermal energy use, Slovakia*.

Bertotti, G., & Barnhoorn, A. (2016). Geology of mode i, hybrid and mode ii fractures-what do we really know? *78th EAGE Conference and Exhibition 2016*, *2016*(1), 1–5.

Bisdom, K., Bertotti, G., & Nick, H. M. (2016). The impact of different aperture distribution models and critical stress criteria on equivalent permeability in fractured rocks. *Journal of Geophysical Research: Solid Earth*, *121*(5), 4045–4063.

Boersma, Q. D., Bruna, P. O., De Hoop, S., Vinci, F., Tehrani, A. M., & Bertotti, G. (2021). The impact of natural fractures on heat extraction from tight triassic sandstones in the west netherlands basin: A case study combining well, seismic and numerical data. *Netherlands Journal of Geosciences*, *100*, e6.

Bofill, L., Bozetti, G., Schäfer, G., Ghienne, J.-F., Schuster, M., Scherer, C., & de Souza, E. (2024). Quantitative facies analysis of a fluvio-aeolian system: Lower triassic buntsandstein group, eastern france. *Sedimentary Geology*, *465*, 106634.

Bond, C. E., Gibbs, A. D., Shipton, Z. K., Jones, S., et al. (2007). What do you think this is¿'conceptual uncertainty"in geoscience interpretation. *GSA today*, *17*(11), 4.

Bond, C. E., Johnson, G., & Ellis, J. (2015). Structural model creation: The impact of data type and creative space on geological reasoning and interpretation. *Special Publications*, *421*(1), 83–97.

Bose, S., & Mitra, S. (2009). Deformation along oblique and lateral ramps in listric normal faults: Insights from experimental models. *AAPG bulletin*, *93*(4), 431–451.

Bossennec, C. M. (2019). *Évolution des propriétés de transfert des grès par diagénèse et déformation: Application aux formations du buntsandstein gp., graben du rhin* [Thèse de doctorat]. Université de Lorraine [Soutenance publique prévue le 24 avril 2019].

Brownstein, N. C., Louis, T. A., O'Hagan, A., & Pendergast, J. (2019). The role of expert judgment in statistical inference and evidence-based decision-making. *The American Statistician*, *73*(sup1), 56–68.

Bruhn, R. L., & Schultz, R. A. (1996). Geometry and slip distribution in normal fault systems: Implications for mechanics and fault-related hazards. *Journal of Geophysical Research: Solid Earth*, *101*(B2), 3401–3412.

Buchanan, P., & McClay, K. (1991). Sandbox experiments of inverted listric and planar fault systems. *Tectonophysics*, *188*(1-2), 97–115.

Caine, J. S., Evans, J. P., & Forster, C. B. (1996). Fault zone architecture and permeability structure. *Geology*, *24*(11), 1025–1028.

Carr, W. (1992). *Structure in continuously cored, deep drill holes at yucca mountain, nevada, with notes on calcite occurrence; yucca mountain site characterization project* (tech. rep.). Sandia National Lab.(SNL-NM), Albuquerque, NM (United States); Carr (Wilfred …

Childs, C., Holdsworth, R. E., Jackson, C. A.-L., Manzocchi, T., Walsh, J. J., & Yielding, G. (2017). Introduction to the geometry and growth of normal faults.

Choi, J.-H., Edwards, P., Ko, K., & Kim, Y.-S. (2016). Definition and classification of fault damage zones: A review and a new methodological approach. *Earth-Science Reviews*, *152*, 70–87.
Congro, M., Zanatta, A. S., Nunes, K., Quevedo, R., Carvalho, B. R., & Roehl, D. (2023). Determination of fault damage zones in sandstone rocks using numerical models and statistical analyses. *Geomechanics for Energy and the Environment*, *36*, 100495.
Cooke, M. (1997). Predicting fracture localization in folded strata from mechanical stratigraphy and fold shape: Case study of east kaibab monocline, utah. *International Journal of Rock Mechanics and Mining Sciences*, *34*(3-4), 56–e1.
Cosgrove, J. W., & Ameen, M. S. (1999). A comparison of the geometry, spatial organization and fracture patterns associated with forced folds and buckle folds. *Geological Society, London, Special Publications*, *169*(1), 7–21.
Cosgrove, J. (1999). Forced folds and fractures: An introduction. *Geological Society, London, Special Publications*, *169*(1), 1–6.
Cosgrove, J. (2015). The association of folds and fractures and the link between folding, fracturing and fluid flow during the evolution of a fold–thrust belt: A brief review.
Cruz, R. A. Q., Cacau, D. C., dos Santos, R. M., Pereira, E. J. R., Leta, F. R., & Clua, E. G. (2017). Improving accuracy of automatic fracture detection in borehole images with deep learning and gpus. *2017 30th SIBGRAPI conference on graphics, patterns and images (SIBGRAPI)*, 345–350.
Curtis, A. (2012). The science of subjectivity. *Geology*, *40*(1), 95–96.
Dèzes, P., Schmid, S. M., & Ziegler, P. A. (2004). Evolution of the european cenozoic rift system: Interaction of the alpine and pyrenean orogens with their foreland lithosphere. *Tectonophysics*, *389*(1-2), 1–33.
Doesburg, M. (2023). *Uncertainty reduction in image log fracture interpretation, and its implications to the geological history of the geneva basin, switzerland* [Master's thesis, Delft University of Technology].
Dula Jr, W. F. (1991). Geometric models of listric normal faults and rollover folds. *AAPG bulletin*, *75*(10), 1609–1625.
EPA. (2025, April). https://www.epa.gov/environmental-geophysics/borehole-formation-microresistivity-imaging-fmi#:~:text=FMI%20logs%20show%20the%20variations,within%20FMI%20logs%20is%20structural.
Evans, J. S. B., & Stanovich, K. E. (2013). Dual-process theories of higher cognition: Advancing the debate. *Perspectives on psychological science*, *8*(3), 223–241.
FindHeat. (2024). https://findheat.eu/
Fossen, H. (2016). *Structural geology*. Cambridge university press.
Genter, A., Castaing, C., Dezayes, C., Tenzer, H., Traineau, H., & Villemin, T. (1997). Comparative analysis of direct (core) and indirect (borehole imaging tools) collection of fracture data in the hot dry rock soultz reservoir (france). *Journal of Geophysical Research: Solid Earth*, *102*(B7), 15419–15431.
GeORG. (2017). Georg mapviewer. https://maps.geopotenziale.eu/?app=georg&lang=en
Gigerenzer, G. (2015). On the supposed evidence for libertarian paternalism. *Review of philosophy and psychology*, *6*, 361–383.
Glaas, C., Vidal, J., & Genter, A. (2021). *Mineralogical and structural controls on permeability of deep naturally fractured crystalline reservoirs. insights from geothermal wells (upper rhine graben)* (tech. rep.). Universite de Strasbourg…
Hancock, P. (1985). Brittle microtectonics: Principles and practice. *Journal of structural geology*, *7*(3-4), 437–457.
Hardy, S., & Allmendinger, R. W. (2011). Trishear: A review of kinematics, mechanics, and applications.
Healy, D., Blenkinsop, T. G., Timms, N. E., Meredith, P. G., Mitchell, T. M., & Cooke, M. L. (2015). Polymodal faulting: Time for a new angle on shear failure. *Journal of Structural Geology*, *80*, 57–71.
Hehn, R., Genter, A., Vidal, J., & Baujard, C. (2016). Stress field rotation in the egs well grt-1 (rittershoffen, france). *Proceedings of European Geothermal Congress*.
Hupkes, J., Bruna, P.-O., Bertotti, G., Doesburg, M., & Moscariello, A. (2025). *A fracture never comes alone: Prediction of associations of fractures and stylolites in naturally fractured carbonate geothermal reservoirs based on analogue outcrops* [Manuscript in preparation], 1: Department of Geoscience and Engineering, Delft University of Technology; 2: Department of Earth Sciences, University of Geneva.
Illies, J. (1972). The rhine graben rift system-plate tectonics and transform faulting. *Geophysical surveys*, *1*(1), 27–60.
Jacques, D., Muchez, P., & Sintubin, M. (2022). Conjugate, riedel-shear vein arrays: A new type of en echelon vein system. *Journal of Structural Geology*, *163*, 104725.
Kianizadeh, N., Rahimi, B., Lashkaripour, G. R., & Fakoor, V. (2021). Kinematic and statistical analysis of fold related fractures in the northeast of kopet dagh folded belt, northeast iran. *Journal of the Geological Society of India*, *97*, 428–441.
Kim, I., Park, S.-I., Kwon, S., & Lee, H.-J. (2022). Evolution of fracture networks and connectivity during fault–bend folding: Insights from the sinon anticline in the southwestern hongseong–imjingang belt, korea. *Journal of Structural Geology*, *155*, 104506.
Kim, Y. S., Peacock, D. C., & Sanderson, D. J. (2004). Fault damage zones. *Journal of structural geology*, *26*(3), 503–517.
Li, Y., Hou, G., Hari, K., Neng, Y., Lei, G., Tang, Y., Zhou, L., Sun, S., & Zheng, C. (2018). The model of fracture development in the faulted folds: The role of folding and faulting. *Marine and Petroleum Geology*, *89*, 243–251.
Macrae, E. J., Bond, C. E., Shipton, Z. K., & Lunn, R. J. (2016). Increasing the quality of seismic interpretation. *Interpretation*, *4*(3), T395–T402.
Mayolle, S., Soliva, R., Caniven, Y., Wibberley, C., Ballas, G., Milesi, G., & Dominguez, S. (2019). Scaling of fault damage zones in carbonate rocks. *Journal of Structural Geology*, *124*, 35–50.
Mayolle, S., Soliva, R., Dominguez, S., & Wibberley, C. (2023). Normal fault damage zone growth in map view from analogue models. *Journal of Structural Geology*, *176*, 104975.
McClay, K., & Scott, A. (1991). Experimental models of hangingwall deformation in ramp-flat listric extensional fault systems. *Tectonophysics*, *188*(1-2), 85–96.
McClay, K., Waltham, D., Scott, A., & Abousetta, A. (1991). Physical and seismic modelling of listric normal fault geometries. *Geological Society, London, Special Publications*, *56*(1), 231–239.
Ofoegbu, G. I., & Ferrill, D. A. (1998). Mechanical analyses of listric normal faulting with emphasis on seismicity assessment. *Tectonophysics*, *284*(1-2), 65–77.
O'Hagan, A. (2019). Expert knowledge elicitation: Subjective but scientific. *The American Statistician*, *73*(sup1), 69–81.
O'Hara, A. P., Jacobi, R. D., & Sheets, H. D. (2017). Predicting the width and average fracture frequency of damage zones using a partial least squares statistical analysis: Implications for fault zone development. *Journal of Structural Geology*, *98*, 38–52.

Peacock, D. C. P., Dimmen, V., Rotevatn, A., & Sanderson, D. (2017). A broader classification of damage zones. *Journal of Structural Geology*, *102*, 179–192.
Pérez-Díaz, L., Alcalde, J., & Bond, C. E. (2020). Introduction: Handling uncertainty in the geosciences: Identification, mitigation and communication. *Solid Earth*, *11*(3), 889–897.
Petrov, A., Egorov, D., Belayouni, N., & Tamaazousti, Y. (2024). Enhanced vuggy zone recognition through merging ai-based borehole image interpretation. *Abu Dhabi International Petroleum Exhibition and Conference*, D021S044R004.
Plenefisch, T., & Bonjer, K.-P. (1997). The stress field in the rhine graben area inferred from earthquake focal mechanisms and estimation of frictional parameters. *Tectonophysics*, *275*(1-3), 71–97.
Price, N. J., & Cosgrove, J. W. (1990). *Analysis of geological structures*. Cambridge University Press.
Resor, P. G., & Pollard, D. D. (2012). Reverse drag revisited: Why footwall deformation may be the key to inferring listric fault geometry. *Journal of Structural Geology*, *41*, 98–109.
Rotevatn, A., Jackson, C. A.-L., Tvedt, A. B., Bell, R. E., & Blækkan, I. (2019). How do normal faults grow? *Journal of Structural Geology*, *125*, 174–184.
Savage, H. M., & Brodsky, E. E. (2011). Collateral damage: Evolution with displacement of fracture distribution and secondary fault strands in fault damage zones. *Journal of Geophysical Research: Solid Earth*, *116*(B3).
Schueller, S., Braathen, A., Fossen, H., & Tveranger, J. (2013). Spatial distribution of deformation bands in damage zones of extensional faults in porous sandstones: Statistical analysis of field data. *Journal of Structural Geology*, *52*, 148–162.
Schumacher, M. E. (2002). Upper rhine graben: Role of preexisting structures during rift evolution. *Tectonics*, *21*(1), 6–1.
Shelton, J. W. (1984). Listric normal faults: An illustrated summary. *AAPG Bulletin*, *68*(7), 801–815.
Skyttä, P., Ovaskainen, N., Nordbäck, N., Engström, J., & Mattila, J. (2021). Fault-induced mechanical anisotropy and its effects on fracture patterns in crystalline rocks. *Journal of Structural Geology*, *146*, 104304.
SLB. (2025). Ultrasonic borehole imager – acoustic imaging [Accessed: 2025-05-30]. https://www.slb.com/products-and-services/innovating-in-oil-and-gas/reservoir-characterization/surface-and-downhole-logging/wireline-openhole-logging/ultrasonic-borehole-imager
Smeraglia, L., Mercuri, M., Tavani, S., Pignalosa, A., Kettermann, M., Billi, A., & Carminati, E. (2021). 3d discrete fracture network (dfn) models of damage zone fluid corridors within a reservoir-scale normal fault in carbonates: Multiscale approach using field data and uav imagery. *Marine and Petroleum Geology*, *126*, 104902.
Smith, R. Y., Bruna, P.-O., Nasri, A., & Bertotti, G. (2024). Fracture distribution along open folds in southern tunisia: Implications for naturally fractured reservoirs. *Petroleum Geoscience*, *30*(1), petgeo2023–039.
Soll, J. B., Milkman, K. L., & Payne, J. W. (2015). A user's guide to debiasing. *The Wiley Blackwell handbook of judgment and decision making*, *2*, 924–951.
Song, T., & Cawood, P. A. (2001). Effects of subsidiary faults on the geometric construction of listric normal fault systems. *AAPG bulletin*, *85*(2), 221–232.
Souque, C., Knipe, R. J., Davies, R. K., Jones, P., Welch, M. J., & Lorenz, J. (2019). Fracture corridors and fault reactivation: Example from the chalk, isle of thanet, kent, england. *Journal of Structural Geology*, *122*, 11–26.
Spahić, D., Exner, U., Behm, M., Grasemann, B., Haring, A., & Pretsch, H. (2011). Listric versus planar normal fault geometry: An example from the eisenstadt-sopron basin (e austria). *International Journal of Earth Sciences*, *100*, 1685–1695.
Special Interest Group AI & Assessment. (2025, March). https://www.tudelft.nl/teaching-support/educational-advice/assess/guidelines/ai-chatbots-in-unsupervised-assessment
Sun, S., Hou, G., & Zheng, C. (2017). Fracture zones constrained by neutral surfaces in a fault-related fold: Insights from the kelasu tectonic zone, kuqa depression. *Journal of Structural Geology*, *104*, 112–124.
Suppe, J., & Medwedeff, D. A. (1990). Geometry and kinematics of fault-propagation folding. *Eclogae Geologicae Helvetiae*, *83*(3), 409–454.
Torabi, A., Alaei, B., & Libak, A. (2019). Normal fault 3d geometry and displacement revisited: Insights from faults in the norwegian barents sea. *Marine and Petroleum Geology*, *99*, 135–155.
Torabi, A., Ellingsen, T., Johannessen, M., Alaei, B., Rotevatn, A., & Chiarella, D. (2020). Fault zone architecture and its scaling laws: Where does the damage zone start and stop?
Ukar, E., Gale, J. F., Fall, A., López, R. G., Hryb, D., Manceda, R., Brisson, I., Hernandez-Bilbao, E., Weger, R. J., Marchal, D. A., et al. (2020). Natural fractures: From core and outcrop observations to subsurface models.
Ukar, E., Laubach, S. E., & Hooker, J. N. (2019). Outcrops as guides to subsurface natural fractures: Example from the nikanassin formation tight-gas sandstone, grande cache, alberta foothills, canada. *Marine and Petroleum Geology*, *103*, 255–275.
Ulutaş, E. (2020). The may 11 paphos, cyprus, earthquake: Implications for stress regime and tsunami modelling for the eastern mediterranean shorelines. *Arabian Journal of Geosciences*, *13*, 970. https://doi.org/10.1007/s12517-020-05943-1
Valley, B., Dezayes, C., & Genter, A. (2007). Multi-scale fracturing in the soultz-sous-forêts basement from borehole image analyses. *Proceedings EHDRA scientific conference*, *28*, 13.
Vidal, J., & Genter, A. (2018). Overview of naturally permeable fractured reservoirs in the central and southern upper rhine graben: Insights from geothermal wells. *Geothermics*, *74*, 57–73.
Vidal, J., Genter, A., & Chopin, F. (2017). Permeable fracture zones in the hard rocks of the geothermal reservoir at rittershoffen, france. *Journal of Geophysical Research: Solid Earth*, *122*(7), 4864–4887.
Vidal, J., Genter, A., & Schmittbuhl, J. (2016). Pre-and post-stimulation characterization of geothermal well grt-1, rittershoffen, france: Insights from acoustic image logs of hard fractured rock. *Geophysical Journal International*, *206*(2), 845–860.
Vidal, J., Hehn, R., Glaas, C., & Genter, A. (2019). How can temperature logs help identify permeable fractures and define a conceptual model of fluid circulation? an example from deep geothermal wells in the upper rhine graben. *Geofluids*, *2019*(1), 3978364.
Wang, J., Yang, X., Zhang, J., Wang, K., Zhang, R., Wang, Q., Ren, B., & Ukar, E. (2023). Subsurface fracture characterization in a folded ultra-deep tight-gas sandstone reservoir: A case study from the keshen gas field, tarim basin, china. *Journal of Structural Geology*, *172*, 104867.
WellCAD. (2024). WellCAD v5.8: Borehole data management and interpretation software [Version 5.8. Released January 30, 2025. URL: https://wellcad.com].
Williams, G., & Vann, I. (1987). The geometry of listric normal faults and deformation in their hangingwalls. *Journal of Structural Geology*, *9*(7), 789–795.

Wilson, C. G., Bond, C. E., & Shipley, T. F. (2019). How can geologic decision-making under uncertainty be improved? *Solid earth*, *10*(5), 1469–1488.

Witter, J. B., Trainor-Guitton, W. J., & Siler, D. L. (2019). Uncertainty and risk evaluation during the exploration stage of geothermal development: A review. *Geothermics*, *78*, 233–242.

Zang, A., Oye, V., Jousset, P., Deichmann, N., Gritto, R., McGarr, A., Majer, E., & Bruhn, D. (2014). Analysis of induced seismicity in geothermal reservoirs–an overview. *Geothermics*, *52*, 6–21.

Zhao, H., Zhang, J., Qu, J., Zhang, B., Yun, L., Niu, P., Hui, J., & Zhang, Y. (2020). Formation of listric normal faults by extensional duplexing: A case study from the active langshan piedmont fault, nw china. *Journal of Structural Geology*, *140*, 104158.

A

Appendix A

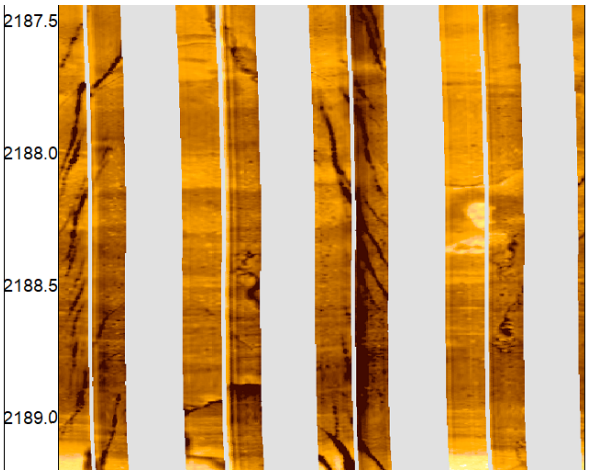

Figure A.1: Example of en echelon fractures at tips of an induced fracture

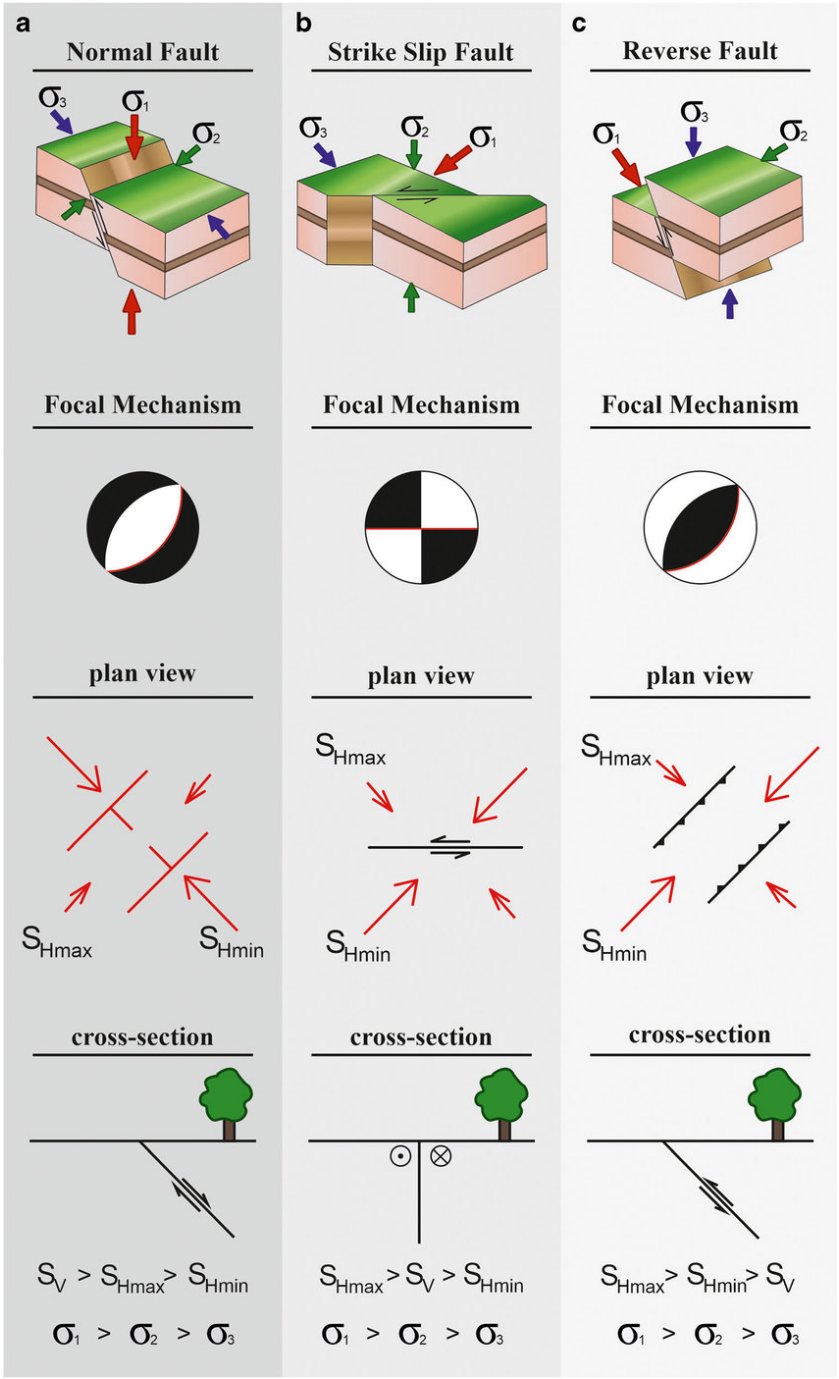

Figure A.2: Overview fault orientations and related stress field (Ulutaş, 2020)

Table A.1: Overview of expected fractures in GRT-1 based on the protocol

Driver	Stress field orientation	Strike	Dip	Type	Frequency	Notes
Farfield - Miocene	NW/SE compression	105.0	85	mode II	very rare	
Farfield - Miocene	NW/SE compression	135.0	85	mode I	very rare	
Farfield - Miocene	NW/SE compression	165.0	85	mode II	very rare	
Farfield - Miocene	NW/SE compression	285.0	85	mode II	very rare	
Farfield - Miocene	NW/SE compression	315.0	85	mode I	very rare	
Farfield - Miocene	NW/SE compression	345.0	85	mode II	very rare	
Farfield - Miocene	NW/SE compression	22.5	60	mode II	common	Sinistral reactivation of graben
Farfield - Miocene	NW/SE compression	202.5	60	mode II	common	Sinistral reactivation of graben
Farfield - Miocene	NW/SE compression	170.0	85	mode I	frequent	Restraining bends between border faults
Farfield - Miocene	NW/SE compression	170.0	60	mode II	frequent	Restraining bends between border faults
Farfield - Miocene	NW/SE compression	350.0	85	mode I	frequent	Restraining bends between border faults
Farfield - Miocene	NW/SE compression	350.0	60	mode II	frequent	Restraining bends between border faults
Farfield - Early Oligocene	NNW/SSE extension	22.5	85	mode I	very frequent	
Farfield - Early Oligocene	NNW/SSE extension	22.5	60	mode II	very frequent	
Farfield - Early Oligocene	NNW/SSE extension	22.5	60	mode II	very frequent	
Farfield - Early Oligocene	NNW/SSE extension	202.5	85	mode I	very frequent	
Farfield - Early Oligocene	NNW/SSE extension	202.5	60	mode II	very frequent	
Farfield - Early Oligocene	NNW/SSE extension	202.5	60	mode II	very frequent	
Farfield - Late Eocene	NNE/SSW compression	22.5	85	mode I	very rare	
Farfield - Late Eocene	NNE/SSW compression	52.5	85	mode II	very rare	
Farfield - Late Eocene	NNE/SSW compression	172.5	85	mode II	very rare	
Farfield - Late Eocene	NNE/SSW compression	202.5	85	mode I	very rare	
Farfield - Late Eocene	NNE/SSW compression	232.5	85	mode II	very rare	
Farfield - Late Eocene	NNE/SSW compression	352.5	85	mode II	very rare	
Farfield - Late Oligocene	NE/SW compression	15.0	85	mode II	very rare	
Farfield - Late Oligocene	NE/SW compression	45.0	85	mode I	very rare	
Farfield - Late Oligocene	NE/SW compression	75.0	85	mode II	very rare	
Farfield - Late Oligocene	NE/SW compression	195.0	85	mode II	very rare	
Farfield - Late Oligocene	NE/SW compression	225.0	85	mode I	very rare	
Farfield - Late Oligocene	NE/SW compression	255.0	85	mode II	very rare	
Farfield - Late Oligocene	NE/SW compression	22.5	60	mode II	common	Dextral reactivation of graben
Farfield - Late Oligocene	NE/SW compression	202.5	60	mode II	common	Dextral reactivation of graben
Farfield - Late Paleaozoic	E(?) compression	112.5	85	mode II	rare	Might be Riedel fractures in Late Variscan orogeny
Farfield - Late Paleaozoic	E(?) compression	112.5	85	mode II	rare	Might be Riedel fractures in Late Variscan orogeny
Farfield - Late Paleaozoic	E(?) compression	112.5	85	mode II	rare	Might be Riedel fractures in Late Variscan orogeny
Farfield - Late Paleaozoic	E(?) compression	292.5	85	mode II	rare	Might be Riedel fractures in Late Variscan orogeny
Farfield - Late Paleaozoic	E(?) compression	292.5	85	mode II	rare	Might be Riedel fractures in Late Variscan orogeny

Continued on next page

Table A.1 – continued from previous page

Driver	Stress field orientation	Depth interval	Strike	Dip	Type	Frequency
Farfield - Late Paleaozoic	E(?) compression	292.5	85	mode II	rare	Might be Riedel fractures in Late Variscan orogeny
Farfield - Late Variscan	E(?) compression	67.5	85	mode II	frequent	Dextral strike slip
Farfield - Late Variscan	E(?) compression	67.5	85	mode II	frequent	Dextral strike slip
Farfield - Late Variscan	E(?) compression	67.5	85	mode II	frequent	Dextral strike slip
Farfield - Late Variscan	E(?) compression	247.5	85	mode II	frequent	Dextral strike slip
Farfield - Late Variscan	E(?) compression	247.5	85	mode II	frequent	Dextral strike slip
Farfield - Late Variscan	E(?) compression	247.5	85	mode II	frequent	Dextral strike slip
Farfield - Middle Eocene	NS compression	0.0	85	mode I	very rare	
Farfield - Middle Eocene	NS compression	30.0	85	mode II	very rare	
Farfield - Middle Eocene	NS compression	150.0	85	mode II	very rare	
Farfield - Middle Eocene	NS compression	180.0	85	mode I	very rare	
Farfield - Middle Eocene	NS compression	210.0	85	mode II	very rare	
Farfield - Middle Eocene	NS compression	330.0	85	mode II	very rare	
Farfield - Middle Eocene	NS compression	52.5	60	mode II	common	Sinistral reactivation of ENE striking shear zones
Farfield - Middle Eocene	NS compression	232.5	60	mode II	common	Sinistral reactivation of ENE striking shear zones
Farfield - Permian	ENE/WSW transpression	112.5	85	mode I	rare	
Farfield - Permian	ENE/WSW transpression	112.5	85	mode I	rare	
Farfield - Permian	ENE/WSW transpression	112.5	85	mode I	rare	
Farfield - Permian	ENE/WSW transpression	292.5	85	mode I	rare	
Farfield - Permian	ENE/WSW transpression	292.5	85	mode I	rare	
Farfield - Permian	ENE/WSW transpression	292.5	85	mode I	rare	
Farfield - Permian	ENE/WSW transpression	90.0	85	mode II	common	
Farfield - Permian	ENE/WSW transpression	90.0	85	mode II	common	
Farfield - Permian	ENE/WSW transpression	90.0	85	mode II	common	
Farfield - Permian	ENE/WSW transpression	135.0	85	mode II	common	
Farfield - Permian	ENE/WSW transpression	135.0	85	mode II	common	
Farfield - Permian	ENE/WSW transpression	135.0	85	mode II	common	
Farfield - Permian	ENE/WSW transpression	270.0	85	mode II	common	
Farfield - Permian	ENE/WSW transpression	270.0	85	mode II	common	
Farfield - Permian	ENE/WSW transpression	270.0	85	mode II	common	
Farfield - Permian	ENE/WSW transpression	315.0	85	mode II	common	
Farfield - Permian	ENE/WSW transpression	315.0	85	mode II	common	
Farfield - Permian	ENE/WSW transpression	315.0	85	mode II	common	
Farfield - Permo-Carboniferous	upwelling intrusive bodies	67.5	85	mode II	very rare	Reactivation of Late Variscan intrusive bodies
Farfield - Permo-Carboniferous	upwelling intrusive bodies	67.5	85	mode II	very rare	Reactivation of Late Variscan intrusive bodies
Farfield - Permo-Carboniferous	upwelling intrusive bodies	67.5	85	mode II	very rare	Reactivation of Late Variscan intrusive bodies
Farfield - Permo-Carboniferous	upwelling intrusive bodies	247.5	85	mode II	very rare	Reactivation of Late Variscan intrusive bodies
Farfield - Permo-Carboniferous	upwelling intrusive bodies	247.5	85	mode II	very rare	Reactivation of Late Variscan intrusive bodies

Continued on next page

Table A.1 – continued from previous page

Driver	Stress field orientation	Depth interval	Strike	Dip	Type	Frequency
Farfield - Permo-Carboniferous	upwelling intrusive bodies	247.5	85	mode II	very rare	Reactivation of Late Variscan intrusive bodies
Farfield - Permo-Carboniferous	N(?) compression	22.5	85	mode II	frequent	Sinistal strike slip. Rhenish shear zone
Farfield - Permo-Carboniferous	N(?) compression	22.5	85	mode II	frequent	Sinistal strike slip. Rhenish shear zone
Farfield - Permo-Carboniferous	N(?) compression	22.5	85	mode II	frequent	Sinistal strike slip. Rhenish shear zone
Farfield - Permo-Carboniferous	N(?) compression	202.5	85	mode II	frequent	Sinistal strike slip. Rhenish shear zone
Farfield - Permo-Carboniferous	N(?) compression	202.5	85	mode II	frequent	Sinistal strike slip. Rhenish shear zone
Farfield - Permo-Carboniferous	N(?) compression	202.5	85	mode II	frequent	Sinistal strike slip. Rhenish shear zone
Rittershoffen fault	NW/SE compression	80.0	30	mode II	very rare	
Rittershoffen fault	NW/SE compression	80.0	30	mode II	very rare	
Rittershoffen fault	NW/SE compression	260.0	30	mode II	very rare	
Rittershoffen fault	NW/SE compression	260.0	30	mode II	very rare	
Rittershoffen fault	NW/SE compression	170.0	60	mode II	frequent	
Rittershoffen fault	NW/SE compression	350.0	60	mode II	frequent	
Rittershoffen fault	NW/SE compression	170.0	85	mode I	frequent	
Rittershoffen fault	NW/SE compression	170.0	85	mode I	frequent	
Rittershoffen fault	NW/SE compression	350.0	85	mode I	frequent	
Rittershoffen fault	NW/SE compression	350.0	85	mode I	frequent	
Rittershoffen fault	NW/SE compression	170.0	60	mode II	frequent	
Rittershoffen fault	NW/SE compression	350.0	60	mode II	frequent	

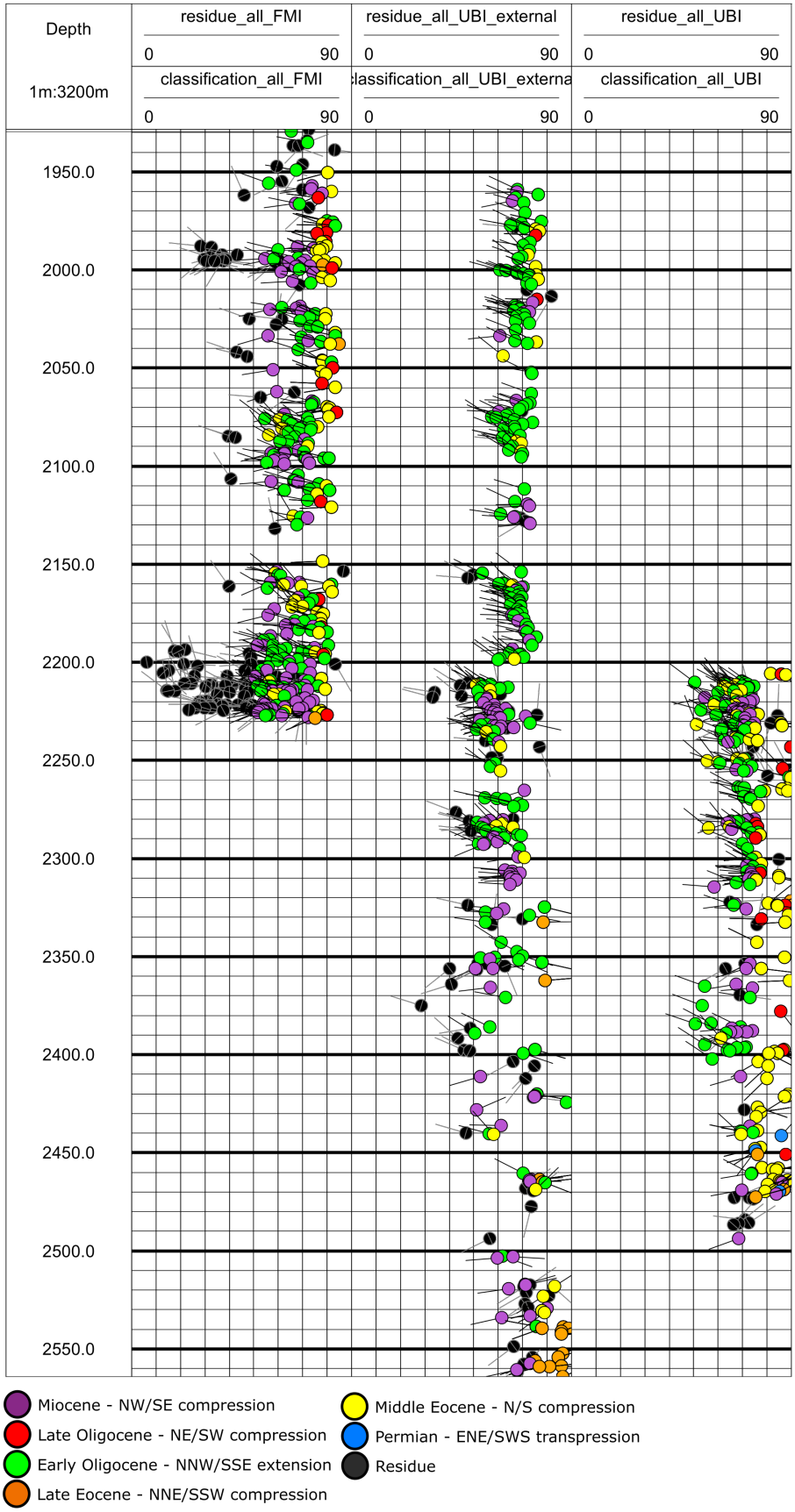

Figure A.3: Classified into drivers, but no agreements over logs.

Figure A.4: Different types of fractures within the Buntsandstein in farfield stress.

B

Appendix B

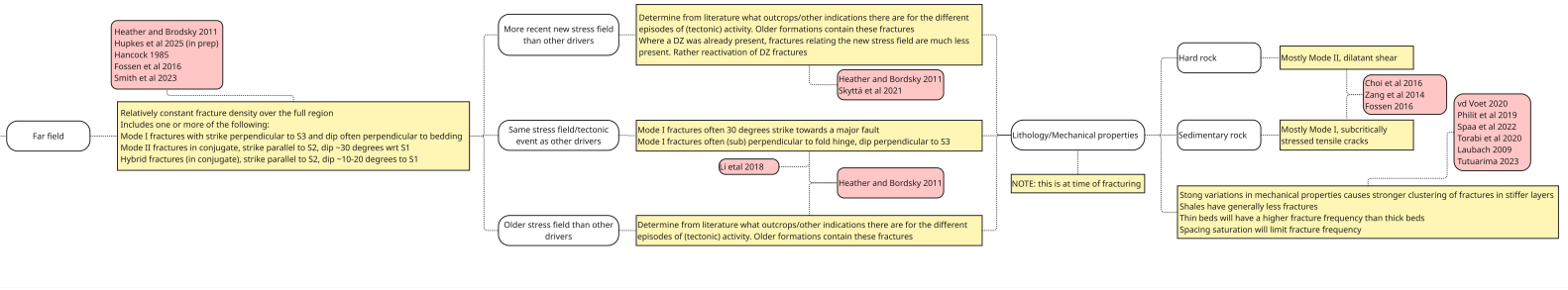

Figure B.1: Pathway in decision tree: far field stresses as driver

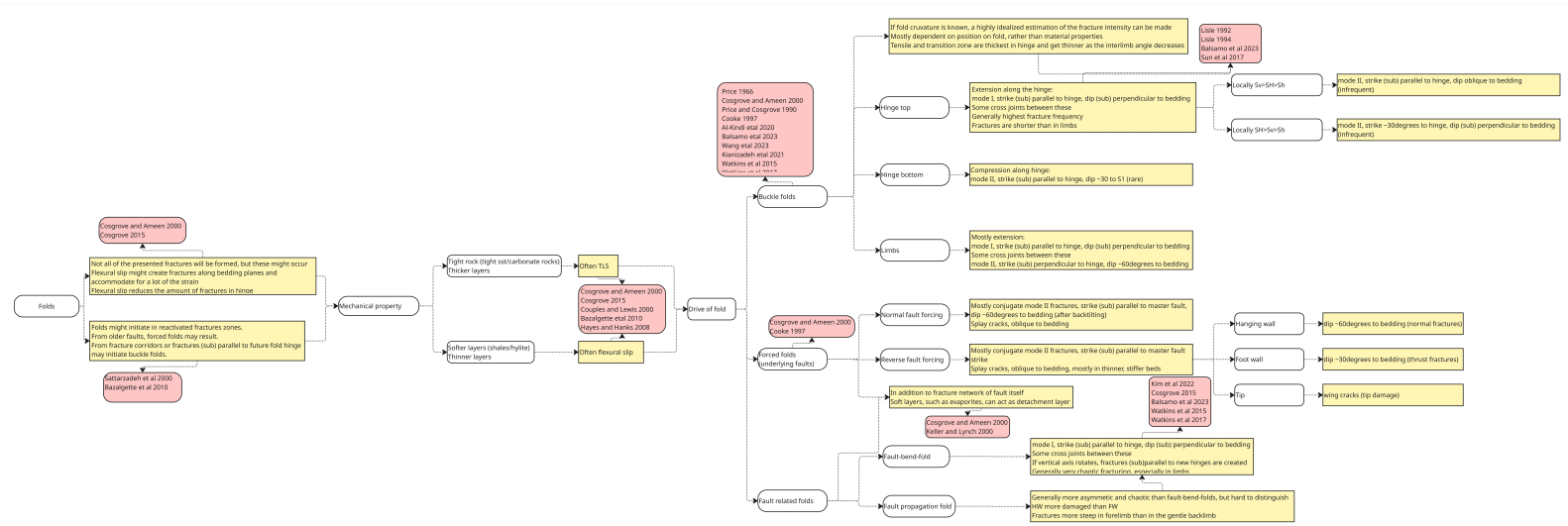

Figure B.2: Pathway in decision tree: folds as driver

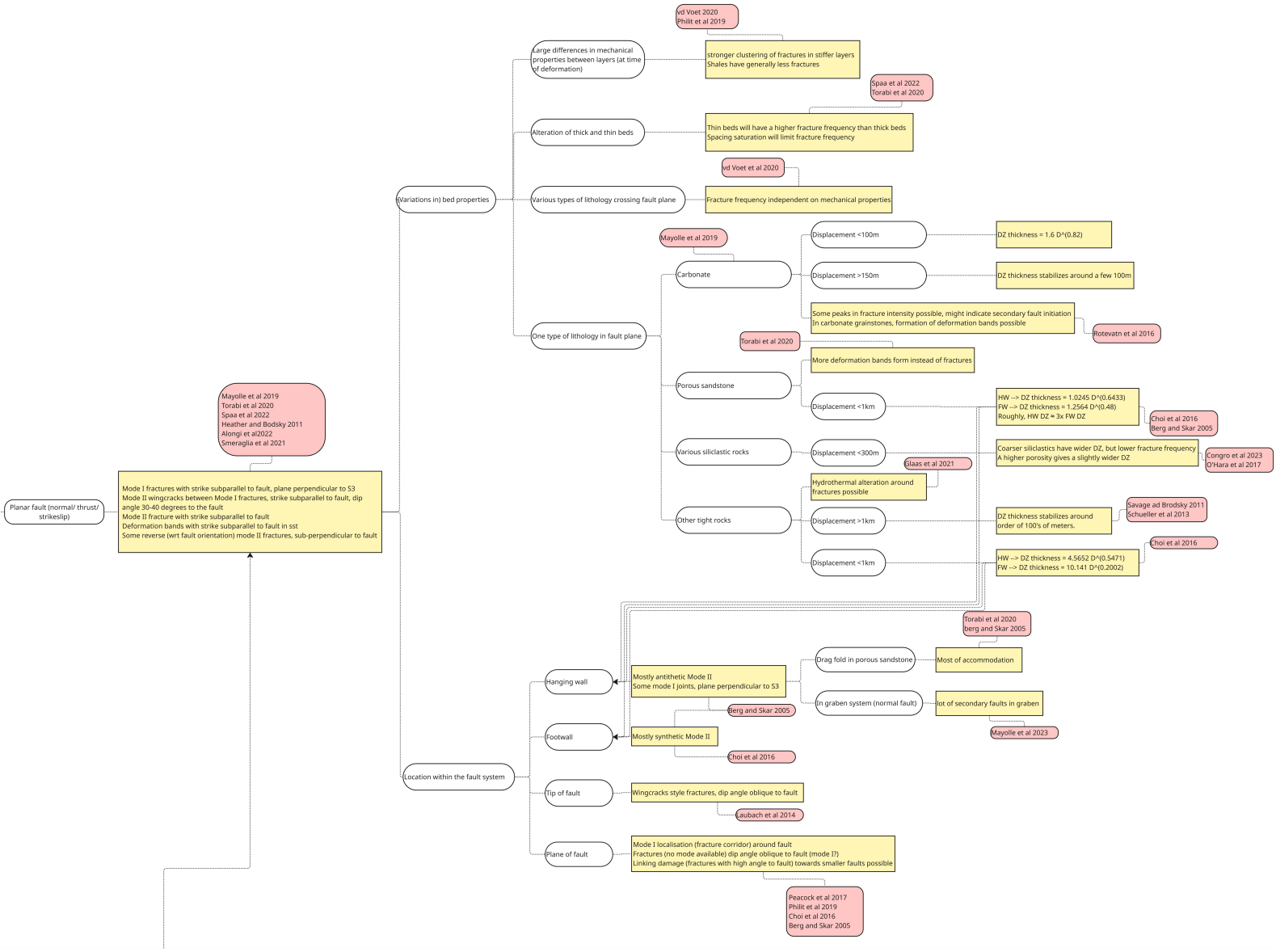

Figure B.3: Pathway in decision tree: planar faults as driver

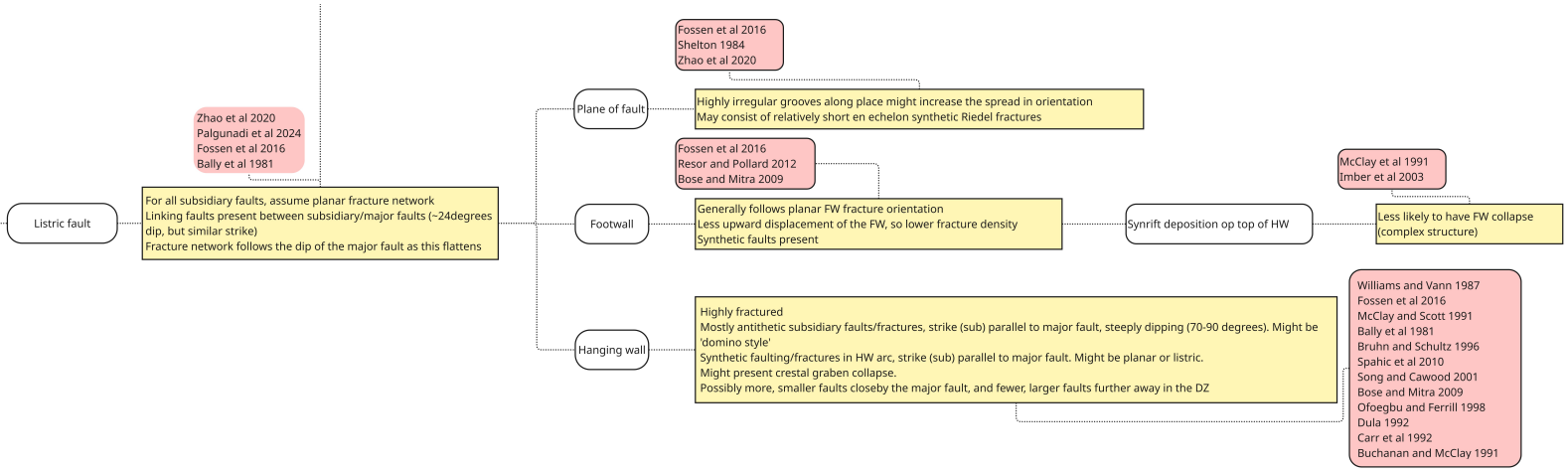

Figure B.4: Pathway in decision tree: listric faults as driver